



**DIFFUSION OF RUBIDIUM VAPOR  
THROUGH HOLLOW-CORE FIBERS FOR  
GAS-PHASE FIBER LASERS**

THESIS

Eric M. Guild, Civilian  
AFIT/OSE/ENP/11-M01

**DEPARTMENT OF THE AIR FORCE  
AIR UNIVERSITY**

***AIR FORCE INSTITUTE OF TECHNOLOGY***

**Wright-Patterson Air Force Base, Ohio**

APPROVED FOR PUBLIC RELEASE; DISTRIBUTION UNLIMITED

The views expressed in this thesis are those of the author and do not reflect the official policy or position of the United States Air Force, the Department of Defense, or the United States Government. This material is declared a work of the U.S. Government and is not subject to copyright protection in the United States.

AFIT/OSE/ENP/11-M01

DIFFUSION OF RUBIDIUM VAPOR THROUGH HOLLOW-CORE FIBERS  
FOR GAS-PHASE FIBER LASERS

THESIS

Presented to the Faculty  
Department of Engineering Physics  
Graduate School of Engineering and Management  
Air Force Institute of Technology  
Air University  
Air Education and Training Command  
in Partial Fulfillment of the Requirements for the  
Degree of Master of Optical Science Engineering

Eric M. Guild, BSEE  
Civilian

March 2011

APPROVED FOR PUBLIC RELEASE; DISTRIBUTION UNLIMITED

AFIT/OSE/ENP/11-M01

DIFFUSION OF RUBIDIUM VAPOR THROUGH HOLLOW-CORE FIBERS  
FOR GAS-PHASE FIBER LASERS

Eric M. Guild, BSEE  
Civilian

Approved:

---

Glen P. Perram, PhD (Chairman)

---

Date

---

Greg A. Pitz, PhD (Member)

---

Date

---

Lt Col Jeremy Holtgrave (Member)

---

Date

## Abstract

This work examines the diffusion of rubidium through a small diameter tube alone and in the presence of noble gases. A fluid dynamics analysis is investigated to aid in choosing a method for transferring atomic rubidium vapor that is reliable and efficient. Solutions to the time dependant ordinary differential equation describing the experimental flow properties of the system reveal more precise outcomes than previously practiced routines. Resolved viscosities and Poiseuille flow theory velocity distributions are characterized for noble gas carriers of the rubidium vapor. Applying Reynolds Numbers to the flow experiments provides pressure differential boundaries that are employed in the successful rubidium vapor transfer process. Atomic spectroscopy is demonstrated through the use of a rubidium  $D_1$  resonate diode laser to record an absorption spectrum and extract alkali vapor number densities that successfully propagated through a 12 *cm* long capillary tube with a 500  $\mu m$  inner diameter. Rubidium number densities on the order of  $1.384 \times 10^{12} \text{ cm}^{-3}$ ,  $4.615 \times 10^{11} \text{ cm}^{-3}$  and  $9.890 \times 10^9 \text{ cm}^{-3}$  were recorded for interaction path lengths of 0.05 *cm*, 0.15 *cm* and 7.0 *cm*, respectively. Number densities were achieved through the constant flow and diffusion of a helium/rubidium combination. Sustaining a constant pressure differential between 80 and 150 *Torr* across the capillary tube assisted in transferring the rubidium vapor through a small inner-diameter hollow-core tube.

AFIT/OSE/ENP/11-M01

*To My Parents*

## Acknowledgements

I would like to thank God for giving me the ability and opportunity to accomplish this work and for providing me with the generous people I have been blessed to work with. I am very grateful for my family for encouraging me throughout my educational process. I would specifically like to thank my parents for pushing me to strive for success and teaching me the virtue of education.

I would like to express my gratitude to my advisor, Dr. Glen Perram, for providing me the opportunity and support in the AFIT graduate program.

I would like to thank the fine people at the Kirtland Air Force Base in New Mexico, Maj Cliff Sulham, David "Tony" Hostutler, Wade Klennert and Don Stalnaker. Without their accommodations, none of this work would have been accomplished.

Additionally, I would like to complement the DPAL research team at AFIT for all of their work, Maj Kirk Brown, Maj Jeffery Gallagher, Capt Edward Hurd Jr., Charlie Fox, Chris Rice and Matthew Lange.

A very special thanks to Greg Pitz who worked with me throughout this entire project.

Finally, my deep appreciation for Lt Col Monte Anderson for his support and teaching skills in the laboratory and for contributing his knowledge and passion for science to my experiences at AFIT.

Eric M. Guild

# Table of Contents

	Page
Abstract .....	iv
Acknowledgements .....	vi
List of Figures .....	viii
List of Tables .....	x
I. Introduction .....	1
The DPAL and Fiber DPAL .....	1
II. Background .....	4
Introduction .....	4
Gas Filled Hollow-Core Fiber Lasers .....	4
Capillary Tube Fluid Dynamics .....	6
Multi-isotopic Rubidium Spectroscopy .....	14
III. Experimental Setup .....	23
Flow Rate Experiments .....	23
Transferring Rubidium Vapor Through a Capillary Tube.....	24
Detecting a Rubidium Spectrum.....	26
IV. Results and Analysis .....	32
Flow Characterization and Viscosity .....	32
Rubidium Number Densities .....	42
V. Conclusions .....	53
Fluid Dynamic Analysis .....	53
Transferring Rubidium Vapor Through a Capillary Tube.....	53
Future Work.....	54
Appendix A. Fitting Inverse Pressure Curves .....	56
Bibliography .....	61



## List of Figures

Figure	Page
1. Heat Pipe Apparatus . . . . .	2
2. Capillary Tube Under Laminar Flow and Tube Cross-Section Dimensions . . . . .	8
3. Simulated Inverse Pressure Curve . . . . .	12
4. $^{85}\text{Rb}$ D <sub>1</sub> Grotrian Diagram . . . . .	17
5. $^{87}\text{Rb}$ D <sub>1</sub> Grotrian Diagram . . . . .	18
6. Hyperfine Transition Relative Amplitudes . . . . .	21
7. Fluid Dynamic Experimental Apparatus . . . . .	24
8. Rubidium Spectroscopy Experimental Apparatus . . . . .	27
9. 20 cm Tube and Laser Beam Location . . . . .	29
10. 12 cm Tube and Laser Beam Location . . . . .	30
11. Flow Rate Data . . . . .	33
12. Diffusion Rates . . . . .	33
13. Inverse Fore Pressure Data . . . . .	34
14. Inverse Pressure Linear Fit Region . . . . .	35
15. Inverse Pressure Linear Fit and Residuals . . . . .	35
16. Inverse Pressure ODE Fit and Residuals . . . . .	37
17. Reynolds Number and Length Down Tube When Laminar Flow Theory is Assumed for Linear Fit . . . . .	38
18. Reynolds Number and Length Down Tube When Laminar Flow Theory is Assumed for ODE Fit . . . . .	38
19. Flow Velocity Profile for Helium . . . . .	40
20. Flow Velocity Profile for Argon . . . . .	41
21. Flow Velocity Profile for Krypton . . . . .	41

Figure	Page
22.	Flow Velocity Profile for Xenon . . . . . 42
23.	Visible Rubidium Deposit . . . . . 44
24.	Rubidium Accumulation Within Capillary Tube . . . . . 44
25.	Color Inverted Image of Rubidium Accumulation Within Capillary Tube . . . . . 45
26.	Rubidium Number Density Spectrum for $\Delta p$ of 80 <i>Torr</i> . . . . . 47
27.	Rubidium Number Density Spectrum for $\Delta p$ of 120 <i>Torr</i> . . . . . 48
28.	Rubidium Number Density Spectrum for $\Delta p$ of 150 <i>Torr</i> . . . . . 48
29.	Transferred Rubidium Spectrum Fit . . . . . 49
30.	Inverse Pressure Linear Fit for Helium . . . . . 57
31.	Inverse Pressure Linear Fit for Argon . . . . . 57
32.	Inverse Pressure Linear Fit for Krypton . . . . . 58
33.	Inverse Pressure Linear Fit for Xenon . . . . . 58
34.	Inverse Pressure ODE Fit for Helium . . . . . 59
35.	Inverse Pressure ODE Fit for Argon . . . . . 59
36.	Inverse Pressure ODE Fit for Krypton . . . . . 60
37.	Inverse Pressure ODE Fit for Xenon . . . . . 60

## List of Tables

Table		Page
1.	Relative Line Strengths and Hyperfine Detuning Frequencies for the D <sub>1</sub> Transition .....	19
2.	Fit and Previous Viscosity Values .....	36
3.	Rubidium Number Densities .....	51
4.	Volume Mixing Ratios .....	51
5.	Linear Fit Parameters .....	56
6.	ODE Fit Parameters .....	56

# DIFFUSION OF RUBIDIUM VAPOR THROUGH HOLLOW-CORE FIBERS FOR GAS-PHASE FIBER LASERS

## I. Introduction

### The DPAL and Fiber DPAL

The United States Air Force has utilized chemical lasers, specifically the chemical oxygen iodine laser (COIL), aboard the Airborne Laser (ABL) and the Advanced Tactical Laser (ATL). Solid state laser systems are also in consideration for such projects, but they introduce thermal management issues. Diode pumped alkali lasers (DPAL) have recently become more attractive because of their high optical-to-optical efficiencies and low thermal loadings. The idea behind DPALs is to turn an unphased diode bars into a powered scaled coherent source. These alkali vapor systems employ a quasi-three level transition scheme where a narrow banded low quality beam excites the valence electron of an alkali vapor atom from the  $^2S_{1/2}$  (ground state) to the  $^2P_{3/2}$  excited ( $D_2$ ) state. A buffer gas, typically ethane or methane, is used to collisionally relax the electron to the  $^2P_{1/2}$  excited ( $D_1$ ) state. If a population inversion is present on the  $D_1$  level, the system will lase down to the ground state. Due to the alkali vapor flowing through the gain cell, thermo-optical distortions may be averted providing an output beam with high beam quality.

Increasing the flow of alkali vapor within the cell has been exercised through the use of a heat pipe to introduce more atom-photon interactions. A heat pipe generates a large number density of alkali vapor in the center of the gain cell. As the temperature of the alkali goes up, the atoms begin to flow to the top of the pipe. Both ends of the

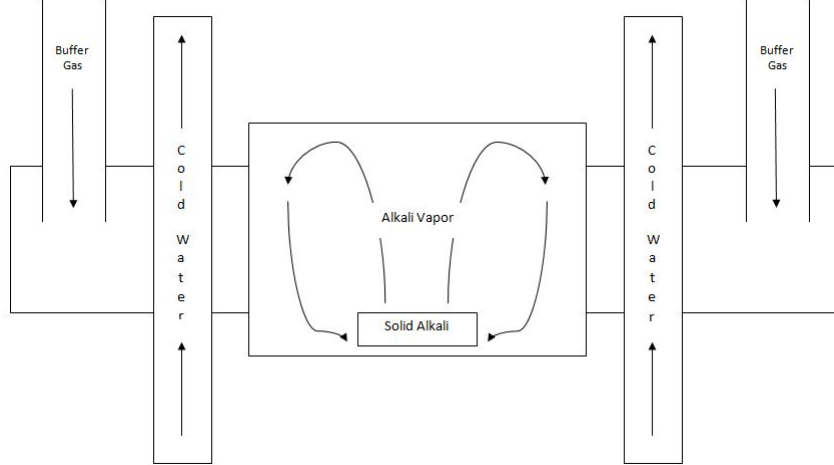


**Figure 1.** Heat pipes were used to generate large number densities of alkali in DPAL systems. The flow of the alkali allows for more atomic-photon interactions. It is created by heating the center of the pipe and cooling the ends with flowing chilled water. Buffer gases are introduced to collisionally relax the excited electrons from the  $^2P_{3/2}$  state to the  $^2P_{1/2}$  state.

heat pipe are sustained around room temperature conditions or slightly lower with the aid of continuously flowing chilled water, which attracts the hot alkali atoms. The alkali experiences a temperature drop as it approaches the ends of the system and will eventually begin to condense and relocate to the bottom of the cell and the process is repeated, as seen in Figure 1. This generates a flowing system within the heat pipe allowing for more alkali-photon interactions throughout the gain medium. Constructing open and closed loop continuously flowing alkali systems is also being investigated to generate more atomic-photon interactions.

Narrowing the diode bars is needed for power scaling. Alkali atomic absorption profiles are extremely narrow requiring the diode emission bandwidth to also be narrowed in order to overlap each other and prevent wasting energy and promote power scaling. Creating a DPAL system within a fiber would create an abundant number of collisions between the alkali atoms and the fiber walls, which would broaden the atomic spectral width. With atomic-fiber wall collisional broadening in consideration,

the requirement to narrow the diode emission bandwidth can be relaxed. Utilizing the waveguide geometries of a fiber would further increase the absorption of the diode because of the large length-to-diameter ratios. The gain medium interaction path distance of a DPAL system could be increased to meters rather than centimeters, which is currently experienced when using free space optics due to the multimode nature and required intensities of the diode. Large amounts of gain over longer distances will be realized from the large surface area to volume ratios characterized by fibers. Combining these characteristics could allow a shorter operating wavelength region and potentially progress to the development of a true hybrid laser system.

## II. Background

### Introduction

This work examines the diffusion of rubidium through a small diameter tube alone and in the presence of noble gases. A diode pumped alkali amplifier laser system can be created if enough alkali vapor is present in the tube. Previous work on hollow-core fiber lasers will be mentioned to explain the different types of lasers that have been demonstrated and the inner diameters that have been used. Understanding the fluid dynamics taking place in the tube will avoid chaotic conditions that produce shock waves that might solidify the alkali vapor. Viscosity measurements are necessary to characterize the flow within the tube and derivations showing how to experimentally extract these values is implemented. Using a carrier gas to assist in transferring rubidium vapor through the capillary tube will be explored. The acquired viscosity values will map a velocity distribution profile determining which gas has the highest flow velocity through the tube while avoiding turbulent flow conditions. An understanding of atomic rubidium spectroscopy is developed in order to calculate the number density of alkali present in the experimental system after the transfer process has occurred.

### Gas Filled Hollow-Core Fiber Lasers

Techniques for generating high number densities of atomic or molecular gases in a fiber are recently in high demand. The practice of filling hollow-core fibers with gases for lasing purposes is unique because it conjoins the techniques of light-atom interactions with the waveguide properties of a fiber. The waveguide geometry of the fiber constrains the light to propagate through the gain medium, such as alkali vapor, over long interaction lengths with little loss due to scatter and transmission through

the fiber. Gas filled fiber lasers also contribute to the concept associated with DPALs of generating a coherent beam from an incoherent source. The cardinal applications for gas filled fibers include atomic spectroscopy, quantum interference, and slow light experiments.

Slepkov et al. [7] generated high rubidium number densities through diffusion inside a 4.5 *cm* long, bare hollow-core photonic band-gap fiber with a core-diameter of 6  $\mu m$ . Number densities on the order of  $10^8 \text{ cm}^{-3}$  were achieved in the fiber using light-induced atomic desorption (LIAD). LIAD is a technique which uses a weak resonate laser to remove measurable atomic densities from an alkali-exposed glass surface. Diffusion processes will be discussed in this thesis in attempt to gain a number density on the order required to operate a DPAL system, which is on the order of  $10^{13} \text{ cm}^{-3}$ . Smith [8] was the first to report a helium-neon laser system within a small inner-diameter (ID) tube in 1971. Using a 20 *cm* long glass capillary tube with a 430  $\mu m$  ID, Smith used a 633 *nm* laser source to create a helium-neon fiber laser. Jin et al. [3] exhibited discharges of argon, helium and carbon dioxide in hollow-core fibers with IDs of 250  $\mu m$ , 150  $\mu m$ , and 50  $\mu m$  and a length up to 13.7 *cm*. Jones et al. [4] demonstrated an optically pumped gas laser in a hollow-core photonic crystal fiber using acetylene ( $C_2H_2$ ). A pulsed source providing 5 – 6 *ns* pulses of approximately 5 *mJ* of energy per pulse was directed into a 1.65 *m* long single-cell optical fiber containing  $C_2H_2$ . A population inversion was confirmed as two rotational branch transitions ((*R*7) and (*P*9)) were observed near 3.12 and 3.16  $\mu m$ . A slope efficiency of a few percent was achieved even though the fiber coupling losses were around 98%. Hostutler et al. [2] demonstrated a rubidium vapor laser with a master oscillator power amplifier. An amplification of 5.9 *dB* and 7.9 *dB* was achieved using a 1.5 *cm* and 2.0 *cm* cell, respectively. The master oscillator performed at a low intensity to avoid saturating the sample. A 14% maximum extraction efficiency



was determined for the alkali amplifier.

## Capillary Tube Fluid Dynamics

As various gases propagate through the capillary tube (a surrogate for a hollow-core fiber) a series of fluid dynamical phenomena occur. Pressure measurements reveal flow characteristics such as diffusion rates, gas viscosity, flow velocity, and flow velocity profiles. Understanding the fluid dynamics will assist in the selection of which gas to choose to efficiently aid in transferring a number density of alkali vapor through a small inner diameter capillary tube. Experimentally determining the gas viscosity requires the ability to model the gas diffusion rate as it flows through the tube. The following derivations discuss how the viscosities can be estimated using variations of the ideal gas law, the geometry of the capillary tube, and the pressure of the chambers on both ends of the tube. The first avenue explores a common technique that assumes a large pressure on the gas inlet side of the tube and a negligible pressure in the aft chamber. The second derivation will include the previously neglected back chamber pressure and outline all of the physical properties occurring in the flow analysis. Once the viscosities are ascertained, the Reynolds Number will be introduced to determine what type of flow is being demonstrated in the tube.

The two most common types of flow for a cylindrical tube, like the one used in this experiment, are turbulent flow and laminar flow. When turbulent flow is present, the gas travels down the pipe in a chaotic and an unpredictable manner with an uneven velocity profile distribution. It is difficult to observe and understand the dynamics of a turbulent flow scenario. Laminar flow theory, also referred to as Poiseuille flow theory, is predictable and provides an easier analysis of the velocity profile distribution. When laminar flow is present, the gas near the center of the capillary tube travels with a higher velocity than on the outer edges of the tube,

represented by  $v(r)$  in Figure 2. Because the wall of the tube is stationary, it applies a small frictional force on the flowing gas. The velocity of the gas at the wall of the tube is zero during laminar flow. The frictional force experienced on the adjacent laminar sheets as they flow by can be described by:

$$f_r = \eta A \frac{dv}{dr} = \eta(2\pi r l) \frac{dv}{dr}, \quad (1)$$

where  $\eta$  is the viscosity of the gas,  $A$  is the area of contact between the laminar sheets,  $l$  is the length of the tube,  $v$  is the flow velocity, and  $r$  is the distance from the center of the capillary tube, making  $\frac{dv}{dr}$  the velocity gradient through the cross-section of the tube. The force driving the fluid through the tube is:

$$f_d = (p_1 - p_2)\pi r^2, \quad (2)$$

where  $p_1$  is the fore pressure and  $p_2$  is the back pressure. When steady flow is observed through the tube, the forces can be described as fully developed and counteract one another when summed together:

$$f_r + f_d = 0 \quad (3)$$

$$\eta(2\pi r l) \frac{dv}{dr} + (p_1 - p_2)\pi r^2 = 0. \quad (4)$$

The fact that the opposing forces sum to zero is a consequence of the law of momentum conservation of the gas propagating through the capillary tube. By solving for the change in the velocity of the gas and reducing the equation the result is:

$$dv = \frac{-(p_1 - p_2)}{2\eta l} r dr. \quad (5)$$

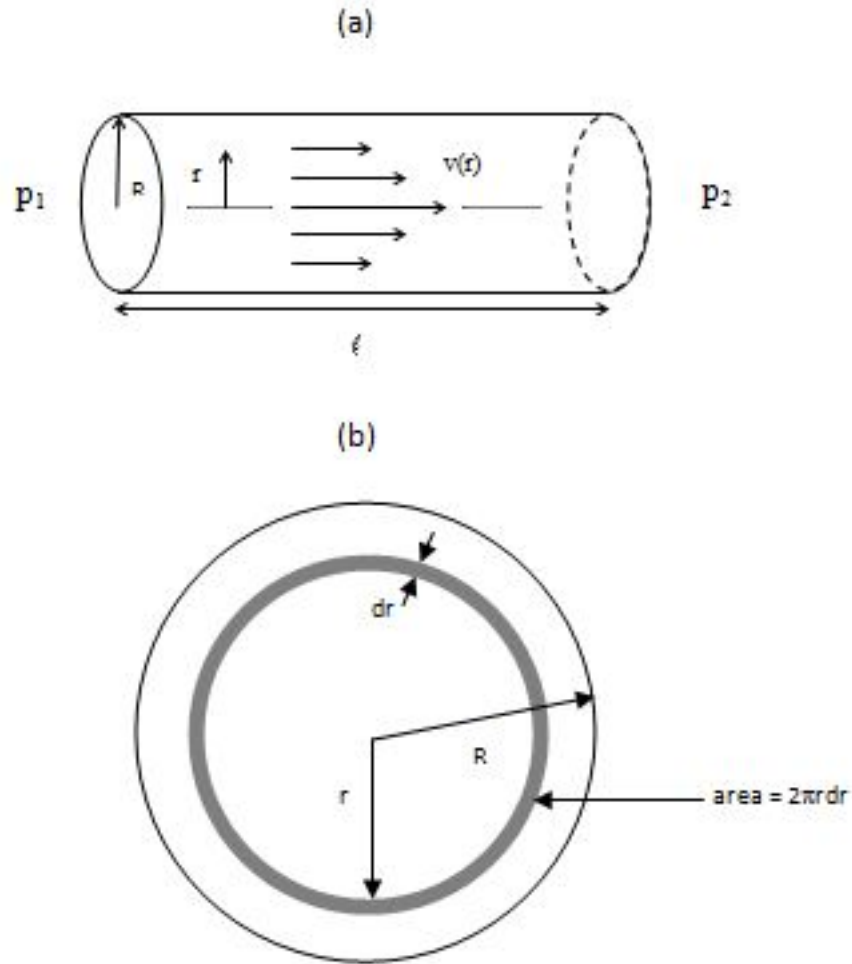


Figure 2. (a) A pipe experiencing a pressure gradient ( $p_1 - p_2$ ) and under laminar flow (Poiseuille flow) has a parabolic velocity profile. The velocity in the center of the tube is the highest and the velocity near the walls is the lowest. As the parabolic profile travels through the capillary tube the gas velocity remains constant along the length of the tube. (b) Cross-section of the capillary tube showing geometrical dimensions.

In order to know the fluid velocity as a function of distance from the center of the capillary tube (*i.e.* the velocity profile distribution) the above equation is integrated from the edge of the pipe to the center of the pipe ( $v = 0$  at  $R = r$ , where  $R$  is the radius of the capillary tube):

$$\int_0^v dv = \frac{-(p_1 - p_2)}{2\eta l} \int_R^r r dr \quad (6)$$

$$v(r) = \frac{(p_1 - p_2)}{4\eta l} (R^2 - r^2). \quad (7)$$

equation (7) describes the gas velocity profile propagating down the center of the tube as a paraboloid when laminar flow is present, shown in Figure 2a. As the parabolic profile travels through the capillary tube the gas velocity remains constant along the length of the tube.

The flow rate through a tube connecting two chambers under a pressure gradient can be found by understanding the geometry of the capillary. By knowing the dimensions of the tube, the volumetric flow rate can be defined as:

$$\frac{dV}{dt} = \int_0^R 2\pi v r dr, \quad (8)$$

where  $V$  is the volume containing the fore pressure. A cross-section of a cylindrical tube is shown in Figure 2b. By substituting equation (7) into equation (8), the change of volume of gas per time becomes:

$$\frac{dV}{dt} = \frac{(2\pi)\Delta p}{4\eta l} \int_0^R r(R^2 - r^2) dr, \quad (9)$$

where  $\Delta p$  is the pressure gradient across the tube,  $(p_1 - p_2)$ . The volumetric flow rate can be reduced to:

$$\frac{dV}{dt} = \frac{\pi(\Delta p)R^4}{8\eta l}. \quad (10)$$

If the average pressure of the system is defined as:

$$\bar{P} = \frac{1}{2}(p_1 + p_2), \quad (11)$$

and if the gas is assumed to be ideal, the number of moles of gas flowing through the tube per unit time is:

$$\frac{dn}{dt} = \frac{\bar{P}}{k_B T} \frac{dV}{dt}, \quad (12)$$

where  $n$  is the number of moles of flowing gas,  $k_B$  is the Boltzmann constant, and  $T$  is the absolute temperature of the system. By substituting in the volumetric flow rate and multiplying by one using the average pressure with the motive of cancellation, the result becomes:

$$\frac{dn}{dt} = \frac{\bar{P}}{k_B T} \frac{\pi \Delta p R^4}{8 \eta l} \frac{(p_1 + p_2)}{2\bar{P}}. \quad (13)$$

Once the gas is added to the fore pressure chamber, it can be assumed that the fore pressure is much greater than the back pressure ( $p_1 \gg p_2$ ) and the flow of gas per unit time is found through:

$$\frac{dn}{dt} = \frac{\pi p_1^2 R^4}{16 k_B T \eta l}. \quad (14)$$

The ideal gas law describes the change of the fore pressure per unit time by:

$$\frac{dp_1}{dt} = \frac{-k_B T}{V} \frac{dn}{dt}, \quad (15)$$

and by inserting equation (14) into equation (15), the statement becomes:

$$\frac{dp_1}{dt} = \frac{-\pi p_1^2 R^4}{16 \eta l V}. \quad (16)$$

The diffusion rate through the capillary tube can be described by the separation of variables in equation (16) and by integrating the fore pressure from the initial pressure

to the instantaneous fore pressure and by integrating over all experimental time. The expression can be written as:

$$-\int_{p_i}^{p_1} \frac{dp_1}{p_1^2} = \frac{\pi R^4}{16\eta l V} \int_0^t dt, \quad (17)$$

which can be simplified to the reciprocal of the fore pressure as:

$$\frac{1}{p_1(t)} = \frac{\pi R^4}{16\eta l V} t + \frac{1}{p_i}, \quad (18)$$

where  $p_i$  is the initial pressure of the system and  $t$  is time. If the geometrical dimensions of the capillary tube are known, the time dependant derivative of equation (18) provides an expression that aids in finding the viscosity of the gas flowing through the tube experimentally:

$$\frac{d(\frac{1}{p_1})}{dt} = \frac{\pi R^4}{16\eta l V}. \quad (19)$$

Figure 3 shows the reciprocal of simulated experimental fore pressure data plotted versus time. The viscosity of the gas can be established by fitting the slope of the initial portion of the inverse fore pressure data. The previous derivations demonstrate a technique for determining the viscosity which will assist in characterizing the type of flow in the capillary tube [5,6].

Rather than exclusively fitting the slope of the inverse pressure, more accurate viscosity results can be extracted by solving the ordinary differential equation that describes the flow through the capillary tube from one chamber to the other. By using the ideal gas law in equation (15) and solving for  $\frac{dn}{dt}$  and inserting the result into equation (13), the expression becomes:

$$\frac{dp_1}{dt} = \frac{\pi(p_1 - p_2)R^4}{8\eta V l} \frac{(p_1 + p_2)}{2}. \quad (20)$$

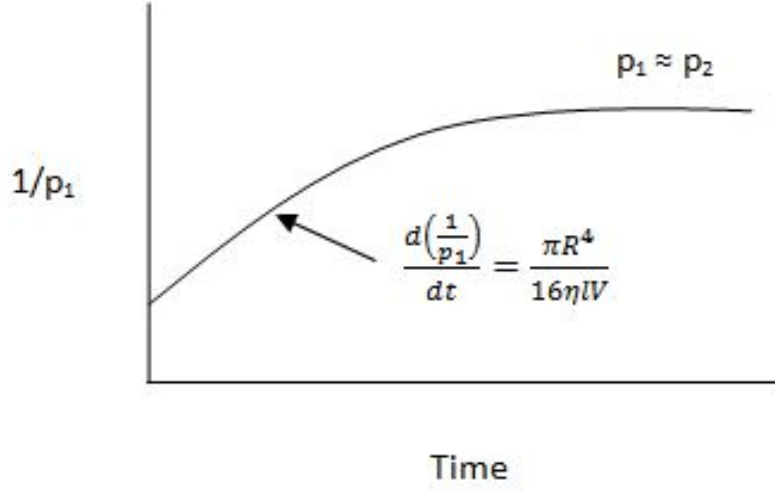


**Figure 3.** Simulated data of the inverse fore pressure plotted versus time. The initial slope of the curve, before the roll-off where the fore pressure is approximately equivalent to the back pressure, provides an analytical expression that can be solved for the flowing gas viscosity.

The assumption where  $p_1 \gg p_2$  will be ignored in order to consider all the physical properties of the system. The pressure that describes the total pressure of the system can be defined by:

$$p_0 = p_1 + p_2. \quad (21)$$

Substituting the back pressure,  $p_2$ , into equation (20), the ordinary differential equation (ODE) describing the fore pressure as a function of time becomes:

$$p_1'(t) = \frac{-\pi(p_1(t) - (p_0 - p_1(t)))R^4}{8\eta V l} \frac{p_1(t) + (p_0 - p_1(t))}{2}. \quad (22)$$

The solution to the ODE is:

$$p_1(t) = \frac{1}{2} \exp\left(\frac{-p_0 \pi R^4 t}{8\eta V l}\right) \left(1 + \exp\left(\frac{p_0 \pi R^4 t}{8\eta V l}\right)\right) p_0. \quad (23)$$

The objective is to fit the entire inverse fore pressure curve which is:

$$\frac{1}{p_1(t)} = \frac{2\exp\left(\frac{p_0\pi R^4 t}{8\eta V l}\right)}{p_0\left(1 + \exp\left(\frac{p_0\pi R^4 t}{8\eta V l}\right)\right)}. \quad (24)$$

Using the MATLAB curve fitting function (which utilizes the Least-Squares, Levenberg-Marquardt, and Gauss-Newton methods) the fit parameters are the total pressure of the system,  $p_0$ , and  $\Gamma$ , where:

$$\Gamma = \frac{\pi R^4}{8\eta V l}. \quad (25)$$

This makes the fit function (with only two fit parameters):

$$\frac{1}{p_1(t)} = \frac{2\exp(p_0\Gamma t)}{p_0\left(1 + \exp(p_0\Gamma t)\right)}, \quad (26)$$

where  $p_0$  is expressed in *Torr* and  $\Gamma$  is expressed in  $(\text{Torr} - \text{Sec})^{-1}$ .

The previous equations demonstrate the derivations leading to discovering the viscosity of the flowing gas as a paraboloid through the center of the capillary tube under the conditions of laminar flow theory. In order to determine whether the flow is turbulent or laminar, the Reynolds Number must be calculated and analyzed for the specific gas under investigation. The Reynolds Number can be found by:

$$Re = \frac{\rho \bar{v} d}{\eta}, \quad (27)$$

where  $\rho$  is the density of the gas,  $\bar{v}$  is the average velocity of the gas through the tube,  $d$  is the diameter of the tube, and  $\eta$  is the viscosity of the gas determined experimentally from equation (19) or equation (26). The average velocity of the gas



is defined as:

$$\bar{v} = \frac{(p_1 - p_2)R^2}{8\eta l}. \quad (28)$$

If the Reynolds Number is less than approximately 30, the Poiseuille flow theory always provides an accurate description of the dynamic flow [10,11]. At higher values of the Reynolds Number, the Poiseuille flow theory applies only after some distance down the tube as it is unlikely the gas enters the tube with the appropriate parabolic velocity profile defined in equation (7). If the Reynolds Number is outside of the Poiseuille flow regime, the distance down the tube before it follows the parabolic velocity profile is calculated by:

$$X \approx \frac{(Re)d}{30}. \quad (29)$$

If the pressure gradient is equivalent for each gas under inspection and the radius and length of the tube are not changed, the maximum velocity of the gases is solely dependent on the viscosity of each gas. Therefore, it is critical to distinguish which type of flow is occurring in the system so that the experimental viscosity results can be confirmed or discarded. The maximum velocity of the gas flowing through the tube is:

$$v_{MAX} = \frac{(p_1 - p_2)R^2}{4\eta}, \quad (30)$$

and can assist in the selection of which gas to choose to efficiently aid in transferring a number density of alkali vapor through a small inner-diameter capillary tube.

## Multi-isotopic Rubidium Spectroscopy

It is imperative to recognize the fundamental quantum principals when investigating an atomic rubidium spectrum. The core objective pertaining to this experiment is to determine the rubidium vapor number density in the capillary tube confirming

a sufficient amount of alkali is present within the tube to generate a diode pumped alkali amplifier. Rubidium has two naturally occurring isotopes,  $^{85}\text{Rb}$  and  $^{87}\text{Rb}$  with abundances 72.17% and 27.83%, respectively. The fine structure of the rubidium atom is defined by coupling the orbital angular momentum,  $L$ , with the spin angular momentum,  $S$ , to provide the total angular momentum of each fine structure energy level,  $J = L + S$ . The energy difference between the fine structure excited states for both isotopes is:

$$E_{fs} = E(^2P_{3/2}) - E(^2P_{1/2}) = 7.123\,020\,683\,THz \pm 60\,kHz. \quad (31)$$

When the total angular momentum is coupled with the nuclear spin,  $I$  ( $I = 5/2$  for  $^{85}\text{Rb}$  and  $I = 3/2$  for  $^{87}\text{Rb}$ ), the hyperfine structure of the rubidium doublet is resolved. The hyperfine structure energy levels follow the quantum selection rules as:

$$|J - I| \leq F \leq J + I, \quad (32)$$

where  $F$  is the total atomic angular momentum. The hyperfine structure energy splitting is defined by:

$$E_{hfs}(F) = E_{fs} + \xi \frac{\chi}{2} + \kappa \frac{(3/2)\chi(\chi + 1) - 2I(I + 1)J(J + 1)}{4I(2I - 1)J(2J - 1)}, \quad (33)$$

where

$$\xi = \frac{\mu_I \bar{H}(0)}{IJ} = \text{magnetic dipole constant}, \quad (34)$$

$$\kappa = eQ\bar{\phi}_{JJ}(0) = \text{electric quadrupole constant}, \quad (35)$$

and

$$\chi \equiv F(F + 1) - I(I + 1) - J(J + 1) = \text{magnetic octupole constant}. \quad (36)$$

It must be noted that the terms in equation (33) containing  $\kappa$  exclusively apply to the energy states with a total angular momentum of  $J = 3/2$  and do not apply to the  $D_1$  transition. The hyperfine structure energy level splitting for both of the rubidium isotopes are shown for the  $D_1$  line in Figure 4 and Figure 5. As a  $D_1$  laser source scans across the resonate transition peaks of the multi-isotopic rubidium vapor, near infrared photo-detectors can be used to capture the atomic absorption spectrum. If the probe intensity is less than the saturation intensity ( $I/I_{sat} < 1$ ) and the sample is not being bleached, the absorbance across the test cell can be described through Beer's Law as:

$$A_\lambda = -\ln(I_t/I_0) = \alpha(\nu, T)l_c = \sigma(\nu, T)N(T)l_c, \quad (37)$$

where  $I_t$  is the transmitted laser intensity through the test cell,  $I_0$  is the intensity of the laser entering the test cell (background intensity),  $\alpha$  is the absorption coefficient,  $\nu$  is the laser frequency,  $T$  is the temperature of the cell,  $l_c$  is the length of the cell,  $\sigma$  is the cross-section of absorption and  $N$  is the rubidium number density in the sample. The  $I/I_0$  data will be extracted from the experiment to determine the absorbance. If the length of the cell is known and the absorption cross-section can be determined, the number density of the system can be ascertained. The cross-section of absorption is found through:

$$\sigma_{F''F'}(\nu, T) = \frac{2\pi^2}{3\epsilon_0 h c} \mu_{F''F'}^2 \nu g(\nu - \nu_{F''F'}), \quad (38)$$

where  $\epsilon_0$  is the vacuum permittivity,  $h$  is Planck's constant,  $c$  is the speed of light in a vacuum,  $\mu_{F''F'}$  is the dipole moment and  $g(\nu - \nu_{F''F'})$  is the absorption lineshape at a resonate frequency transition  $\nu_{F''F'}$  or  $\nu_0$ . The dipole moment can be found by applying the dipole moment operator on the hyperfine transition under investigation:

$$\mu_{F''F'}^2 = S_{F''F'} |\langle J'' || e\mathbf{r} || J' \rangle|^2 = S_{F''F'} e^2 D_{J''J'}^2. \quad (39)$$

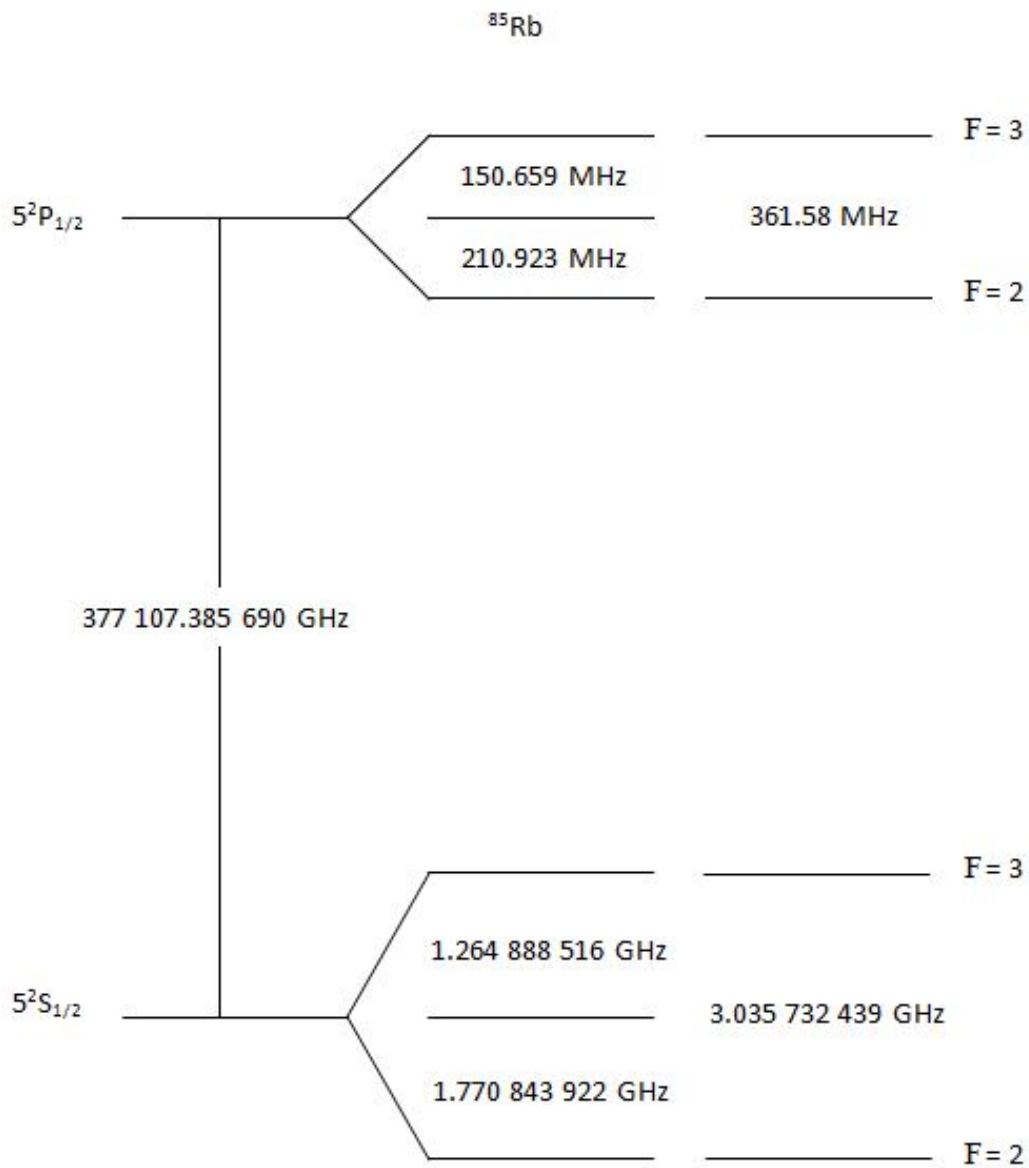


Figure 4. The Grotrian diagram for the  $^{85}\text{Rb}$  D<sub>1</sub> line is shown including the hyperfine structure and energy level splitting frequencies [9].

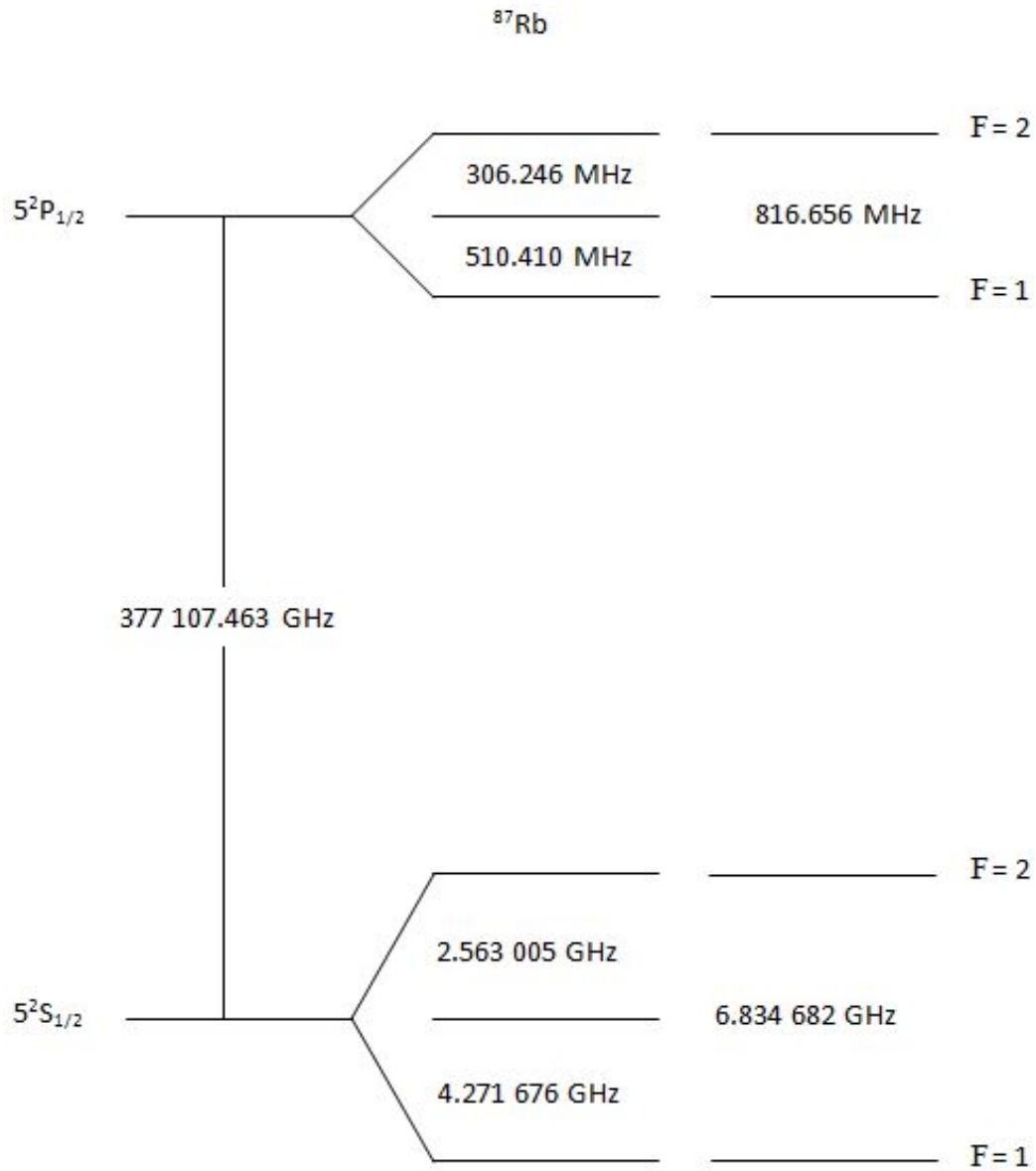


Figure 5. The Grotrian diagram for the  $^{87}\text{Rb}$  D<sub>1</sub> line is shown in including the hyperfine structure and energy level splitting frequencies [9].

The relative line strength,  $S_{F''F'}$ , is resolved using Wigner's 6-j matrix following:

$$S_{F''F'} = (2F' + 1)(2J'' + 1) \left\{ \begin{matrix} J'' & J' & 1 \\ F' & F'' & I \end{matrix} \right\}^2. \quad (40)$$

Relative line strengths with their associated upper ( $F'$ ) and lower ( $F''$ ) hyperfine states are defined for each isotope in Table 1. The dipole moment is used to ascer-

**Table 1. Hyperfine transitions following quantum selection rules for the total atomic angular momentum (equation (32)) for each isotope are associated with a line strength ( $S_{F''F'}$ ) and a detuning frequency ( $\nu - \nu_0$ ) [9]**

	$S_{F''F'}$ (unitless)	$\nu - \nu_0$
<b><sup>85</sup>Rb</b>		
$F'' = 2, F' = 3$	0.778	$1.921\,502\text{ GHz} \pm 71\text{ kHz}$
$F'' = 2, F' = 2$	0.222	$1.559\,920\text{ GHz} \pm 99\text{ kHz}$
$F'' = 3, F' = 3$	0.444	$-1.114\,229\text{ GHz} \pm 71\text{ kHz}$
$F'' = 3, F' = 2$	0.556	$-1.475\,811\text{ GHz} \pm 99\text{ kHz}$
<b><sup>87</sup>Rb</b>		
$F'' = 1, F' = 2$	0.833	$4.577\,922\text{ GHz} \pm 11\text{ kHz}$
$F'' = 1, F' = 1$	0.167	$3.761\,266\text{ GHz} \pm 19\text{ kHz}$
$F'' = 2, F' = 2$	0.500	$-2.256\,759\text{ GHz} \pm 11\text{ kHz}$
$F'' = 2, F' = 1$	0.500	$-3.073\,415\text{ GHz} \pm 19\text{ kHz}$

tain the radiative lifetime of the each energy level of the rubidium atom, but, the degeneracy must be considered to differentiate the levels. The arithmetic to calculate the dipole moment can be quite involved, but can become relatively trivial when the dipole moment is substituted for the radiative lifetime. In terms of the dipole moment, the radiative lifetime is:

$$\frac{1}{\tau_r} = \frac{\omega_0^3}{3\pi\epsilon_0\hbar c^3} \frac{g_{J''}}{g_{J'}} e^2 D_{J''J'}^2, \quad (41)$$

where  $\omega_0$  is the resonate angular frequency ( $\omega_0 = 2\pi\nu_0$ ),  $\hbar$  is Planck's constant divided by  $2\pi$ , and  $g_J$  is the degeneracy of the energy level,  $J$ . This simplifies the dipole

moment to become:

$$\mu_{F''F'}^2 = \frac{3\epsilon_0 \hbar c^3}{16\pi^3 \nu_0^3} \left( \frac{2J' + 1}{2J'' + 1} \right) S_{F''F'} \frac{1}{\tau_r}, \quad (42)$$

and the cross-section of absorption reduces to:

$$\sigma_{F''F'}(\nu, T) = \frac{c^2}{8\pi} \frac{\nu}{\nu_0^3} \left( \frac{2J' + 1}{2J'' + 1} \right) S_{F''F'} \frac{1}{\tau_r} g(\nu - \nu_0). \quad (43)$$

The Boltzmann distribution considers the probability for a single rubidium atom to be excited to one of the hyperfine structure energy states that are shown in Figure 4 and Figure 5. These probabilities are based on the atomic structure and degeneracies of the atom as well as the lower hyperfine energy level of the transition. The Boltzmann distribution can be expressed by:

$$f_{F''} = \frac{(2F'' + 1)e^{-E_{F''}/k_B T}}{\sum_{F''} (2F'' + 1)e^{-E_{F''}/k_B T}}, \quad (44)$$

where  $E_{F''}$  is the energy difference of the  $5^2S_{1/2}$  hyperfine quantum splitting and  $F''$  is the total atomic angular momentum of the lower transition state. The relative amplitude for absorbance,  $-\ln(I_t/I_0)$ , for each resonate transition is simply the product of the line strength,  $S_{F''F'}$ , the Boltzmann distribution,  $f_{F''}$ , and the natural isotopic abundance. The relative amplitudes of each transition are shown in Figure 6 at room temperature and will assist in fitting the acquired rubidium spectrum. Inserting the distribution across all of the possible resonate energy states reduces the total cross-section of absorption to:

$$\sigma(\nu, T) = \sum_{F'', F'} f_{F''} S_{F''F'} \frac{1}{\tau_r} \frac{c^2}{4\pi} \frac{\nu}{\nu_0^3} g(\nu - \nu_0). \quad (45)$$

The lineshape of the atomic transitions can be expressed by the Voigt profile

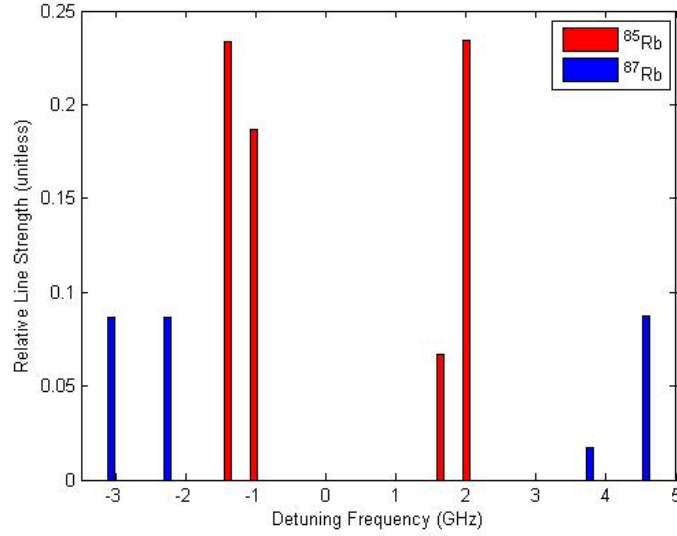


**Figure 6.** Relative frequency locations ( $\nu - \nu_0$ ) and relative amplitudes for each hyperfine transition at room temperature. The relative amplitude is the product of the line strength,  $S_{F''F'}$ , the Boltzmann distribution,  $f_{F''}$ , and the natural isotopic abundance.

approximation:

$$g_V(\nu - \nu_0) = \int_{-\infty}^{\infty} g_I(\nu'_0 - \nu_0) g_H(\nu - \nu'_0) d\nu'_0, \quad (46)$$

which contains a homogeneous and an inhomogeneous part [1]. The homogeneous part contains information about the natural linewidth of the atom and any pressure broadening experienced in the system:

$$g_H(\nu - \nu_0) = \frac{\Delta\nu_H/2\pi}{(\Delta\nu_H/2)^2 + (\nu - \nu_0)^2}, \quad (47)$$

where the full-width at half maximum (FWHM) is illustrated by a Lorentzian line-shape denoted by:

$$\Delta\nu_H = \frac{1}{2\pi} \left( \frac{1}{\tau_r} \right) + \sum_i \gamma_i \left( \frac{T}{T_{data}} \right)^{1/2} P_i. \quad (48)$$

The pressure broadening factor contains the broadening coefficient,  $\gamma_i$ , the temperature at which the broadening coefficients were calculated in order to ration the amount



of broadening,  $T_{data}$ , and the pressure of the system,  $P_i$ .

The inhomogeneous portion of the Voigt profile approximation can be determined from:

$$g_I(\nu - \nu_0) = \frac{2}{\Delta\nu_G} \sqrt{\frac{\ln 2}{\pi}} \exp \left[ -4 \ln 2 \left( \frac{\nu - \nu_0}{\Delta\nu_G} \right)^2 \right], \quad (49)$$

which is represented by a Gaussian lineshape and the FWHM is presented as:

$$\Delta\nu_G = \nu_0 \left( \frac{8k_B T \ln 2}{Mc^2} \right), \quad (50)$$

where  $M$  is the atomic mass of rubidium ( $^{85}\text{Rb} = 1.409 \times 10^{-25} \text{ kg}$ ,  $^{87}\text{Rb} = 1.4432 \times 10^{-25} \text{ kg}$ ) [9]. The Voigt profile is the convolution of the Lorentzian and Gaussian lineshapes. With the system lineshape, the absorption cross-section in equation (45) can be solved using known experimental and spectroscopic information [1]. The low pressure cross-section at line center,  $\sigma_0 = 1.081\,257\,448\,975 \times 10^{-9} \pm 54 \times 10^{-21} \text{ cm}^2$ , will be used to assist in resolving a number density. Experimental procedures will provide the amount of absorbance,  $A_\lambda$ , and the alkali vapor number density generated in each chamber can be extracted using equation (37). If a number density can be extracted from the alkali chambers at each end of the capillary tube, a steady number density gradient can be assumed across the tube to determine whether an alkali amplifier is feasible.

### III. Experimental Setup

#### Flow Rate Experiments

Understanding the fluid dynamics of various gases as they propagate through the capillary tube will assist in choosing the most efficient carrier for the rubidium vapor. By determining the Reynolds Numbers and confirming the flow is characterized by Poiseuille flow theory, shock waves and chaotic flow behavior common during turbulent flow conditions are averted. Shock waves have the potential of solidifying the rubidium if large enough pressures are present within the tube. Before the rubidium was added to the experiment, flow rates were observed from four of the noble gases.

Two stainless steel cubic chambers with an internal volume of  $158.79\text{ cm}^3$  were joined together by a 12 cm long, quarter inch diameter Polymicro glass rod with a  $500\text{ }\mu\text{m}$  hole through the center (#TQNC5006350/200), displayed in Figure 7. The rod was conjoined to the steel cubes using an Ultra-Torr-to-conflat adapter so both ends of the rod were located in the center of the chambers. A lecture bottle gas rack was fabricated in a fashion so helium, argon, krypton, and xenon could be added at separate times by turning the appropriate shut-off valves. The main bus of the noble gases was attached to the top of one of the cubes acting as the fore pressure chamber and the gases could be added gradually using a needle valve. The top of the back pressure cube was affixed to a Varian turbo pump that achieved pressures as low as  $60\text{ nTorr}$ . The vent of the turbo pump was connected to a roughing pump that disposed of the gases pumped out of the system. Two  $1000\text{ Torr}$  MKS Baratron (type 631) pressure sensors were attached to the top of each cube and were wired to a PC using a National Instruments ( $NI - USB - 6221$ ) DAQ, which recorded the pressure of each cube simultaneously using LabView. Using shut-off valves, each chamber could be isolated from the gas inflow and turbo pump, respectively.

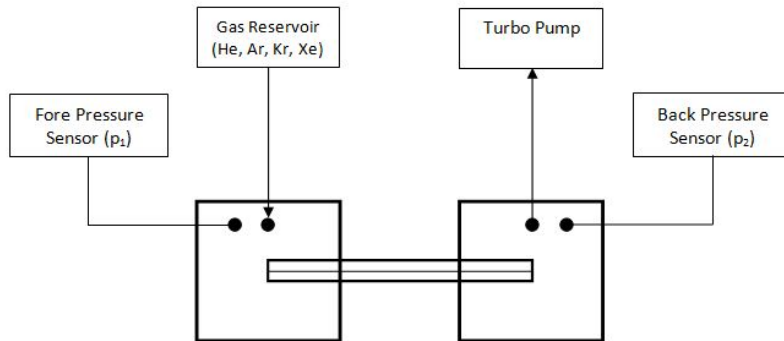


**Figure 7.** Fluid dynamics experimental setup with a 12 *cm* long, quarter inch Polymicro glass rod with a 500  $\mu\text{m}$  hole through the center. Each end of the tube is located in the center of both chambers. Two 1000 *Torr* MKS Baratron (type 631) pressure sensors were attached to the top of each chamber. A gas line capable of dispensing four noble gases was attached to the top of the fore pressure cube and a Varian turbo pump was attached to the top of the back pressure cube.

A leak check was conducted by connecting the system to a helium leak detector and dispensing helium on all of the connections of the system until there were no apparent leaks. The back pressure chamber was pumped down to low pressures then was shut off from the turbo pump. An initial pressure of each gas was added to the fore pressure chamber at different times. The gas diffused through the glass rod filling the back pressure cube until both were at equilibrium. Pressures from both volumes were recorded during the diffusion process.

### Transferring Rubidium Vapor Through a Capillary Tube

Nobel gases were introduced into the fore pressure cube using the gas rack described previously. The gases were proposed as potential carriers to aid in transferring rubidium vapor atoms through the tube and into the pump side chamber. Generating a large alkali vapor number density for the diffusion process required heating the system to temperatures ranging from 60 *C* to 150 *C*. Heating the cubes and capillary tube as uniformly as possible was essential to ensure no rubidium accumulated in cold

areas of the system. A steel housing was placed around the system with six radiating heaters affixed in a formation to adequately increase the temperature of the chambers and the capillary tube in a uniform manner. Both of the chambers were placed on half-inch thick metal plates. Each plate contained four equally spaced holes burrowed horizontally with diameters just large enough for current driven heater elements to be inserted. The heater elements and resistance temperature detectors (RTD) placed on the bottom of each plate were connected to a modified Watlow heater controller that prevented increasing and decreasing temperature ramping. Thermocouples probed the interior of the housing allowing an accurate temperature reading of the radiation being projected onto the exterior of the cubes and capillary tube. Calcium fluoride windows were positioned in six locations where diode laser beams entered or exited the system. A cold trap filled with liquid nitrogen was placed at the exit of the back pressure chamber as a safety net to solidify and condense any rubidium atoms before reaching the turbo pump. The vent of the turbo pump was connected to a roughing pump to dispose of the substances extracted from the experimental apparatus.

Once the system was heated to create rubidium vapor, three techniques were demonstrated with the main goal of transferring the alkali through the capillary tube and into the pump side chamber. The first procedure was to continuously pump on the back pressure chamber with the turbo pump while the fore pressure chamber exclusively contained rubidium vapor. The second routine exploited basic diffusion principals through the inclusion of some noble gases (He, Ar, Kr and Xe). After pumping the system down to low pressures ( $mTorr$ ), the gases were independently added to the fore pressure chamber combining with the alkali and diffusing to the pump side cube. The third approach consolidated the two previously discussed concepts. A noble gas was continually introduced to the fore pressure chamber containing the alkali vapor while the valve to the turbo pump was slightly opened on the pump

side. Keeping both input gas and output pump gateways barely open maintained a deliberate pressure gradient across the capillary tube that was sustained by adjusting the needle valves as necessary. A mixture of the alkali and the noble gas flowed continuously through the tube and into the pump side chamber. Each of these avenues were explored and each achieved their own rates of success.

## Detecting a Rubidium Spectrum

A diode laser was employed to scan across the rubidium  $D_1$  resonance peaks (approximately  $795\text{ nm}$ ) and was driven by a Newport diode driver (560B) and a Thor-Labs temperature controller (TED200). The diode output  $80\text{ mW}$  of power with a spectral linewidth FWHM of  $2\text{ MHz}$  and has a spot size of approximately  $0.5\text{ cm}$ . The saturation intensity for rubidium is  $4.4876 \pm 0.0031\text{ mW/cm}^2$ , which will introduce complications when fitting the spectrum and will be discussed later. A signal generator supplied 50/50 ramp function that was applied to the diode driver at a frequency of  $400\text{ Hz}$  with a peak-to-peak voltage of  $40\text{ mV}$ . These settings ensured the diode would continuously scan forwards and backwards across the rubidium  $D_1$  absorption spectrum. The diode temperature controller was altered to view various areas of the spectrum if desired. The signal generator trigger output was connected to a  $300\text{ MHz}$  oscilloscope to monitor the spectrum. Polarization beam splitters (PBS) were used to direct the beam into four New Focus large-area infrared photoreceivers (2033), as seen in Figure 8. A half-wave plate centered at the diode wavelength was inserted before each PBS to adjust the polarization of the beam. By adjusting the polarization with the half-wave plate, the amount of power ( $< 20\text{ mW}$ ) projected on each detector could be modified to avoid transient broadening and saturating the photoreceivers. The half-wave plates were turned such that identical signals were being displayed on the oscilloscope using the isolated beam with no spectrum being

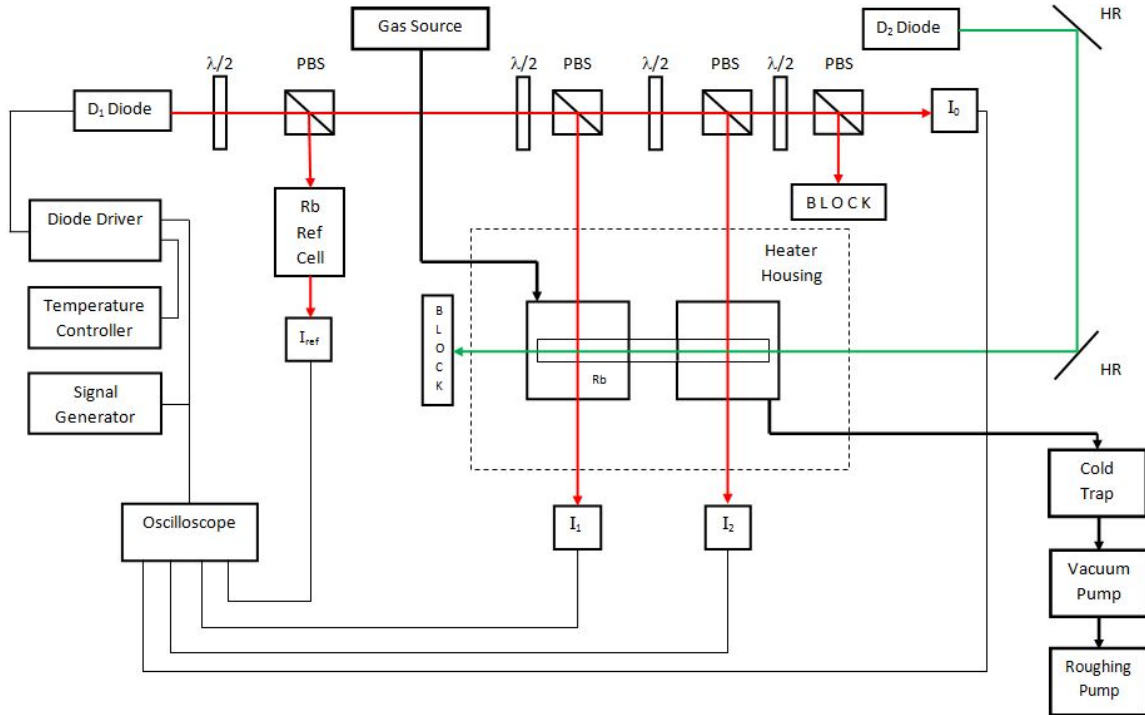
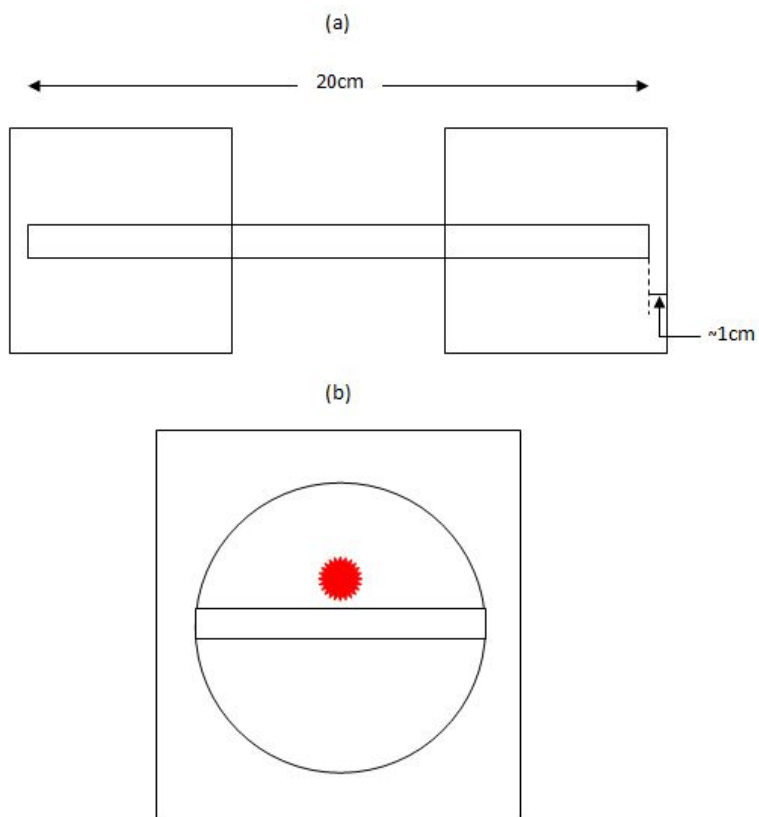


Figure 8. Experimental apparatus used to observe if rubidium vapor diffused through the capillary tube into the pump side chamber. The red lines designate the  $D_1$  diode laser and the green lines represent the  $D_2$  diode laser (the color of the lines are not reflective on the frequency of the lasers but simply to differentiate where each laser was directed).

collected. A low pressure rubidium reference cell containing  $^{87}\text{Rb}$  was used to confirm the laser scanning frequency and assist in finding the  $\text{D}_1$  spectrum. The detector receiving the transmitted signal from the reference cell,  $I_{ref}$ , was connected to the oscilloscope. A second PBS directed the scanning beam into the fore pressure chamber containing both isotopes of rubidium in their natural abundances. The light transmitted through the fore pressure chamber was collected by a different photoreceiver,  $I_1$ . Another PBS was introduced guiding the laser into the back pressure chamber in order to reveal if any rubidium successfully diffused through the tube and into the pump side chamber using a detector,  $I_2$ . A fourth photoreceiver,  $I_0$ , captured the initial scanning laser light and was used to determine the alkali vapor number density through Beer's Law in equation (37).

Two experiments were conducted using two different capillary tube lengths. The first tube used was 20 *cm* long and the ends of the tube were positioned approximately 1 *cm* from the edges of each chamber, displayed in Figure 9a. As shown in Figure 9b, to avoid clipping the capillary tube as the laser propagated through the chambers, the beam was directed above the tube. The second experiment used a 12 *cm* long capillary tube and the ends were located approximately in the center of each chamber, displayed in Figure 10a. For this case, the beams were directed approximately 0.5 *cm* away from the ends of the tube, shown in Figure 10b. A Tiger diode laser tuned at the rubidium  $\text{D}_2$  resonate frequency (approximately 780 *nm*) with a beam diameter of approximately 0.25 *cm* was aligned through the 500  $\mu\text{m}$  inner-diameter capillary tube using two highly-reflective (HR) mirrors. Because of the small diameter of the capillary tube, only about 4% of the beam was coupled into the tube. The 400 *mW* diode source acted as a possible ablation mechanism for any rubidium atoms interacting with pre-existing contaminants formulating on the inner-walls of the capillary tube. A higher power ablation source is commonly utilized, but the Tiger diode laser



**Figure 9.** (a) 20 *cm* long capillary tube location with both ends approximately 1 *cm* from the edges of the chambers. (b) Location of the  $D_1$  scanning laser beam in relation to the capillary tube.



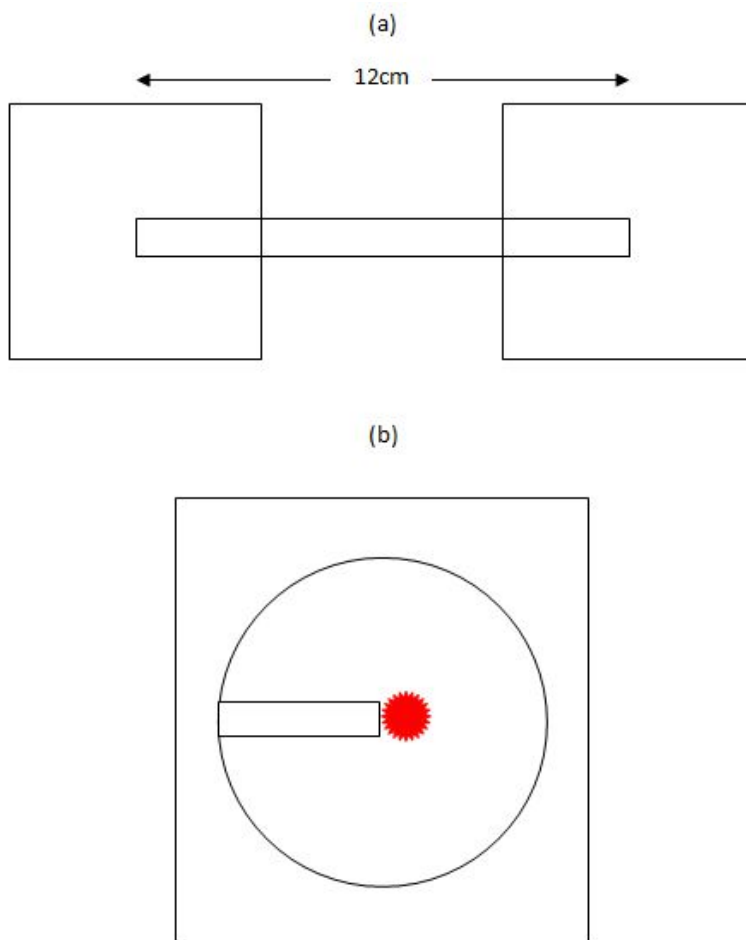


Figure 10. (a) 12 *cm* long capillary tube location with both ends located near the center of the chambers. (b) Location of the  $D_1$  scanning laser beam in relation to the capillary tube.

satisfied the tuning and readily availability requirements. The two HR mirrors were fine-tuned until the majority of the light propagated down the tube with minimal transmission losses.

## IV. Results and Analysis

### Flow Characterization and Viscosity

The viscosity of a gas confirms the type of flow through the capillary tube. Diffusion rates for each gas exploit important pressure differential limits that must be considered. Remaining within the boundaries will ensure laminar flow and avoid jeopardizing the gaseous state of the rubidium. Once a controlled flow environment is implemented, velocity profile distributions can be formed. The flow profiles reveal which gas propagates through the capillary tube with the largest velocity while remaining within the constraints of Poiseuille flow theory.

In four separate experiments, approximately 600 *Torr* of a noble gas was added to the fore pressure chamber. As the gas diffused through the glass rod, the pressure decrease/increase of both chambers was recorded by the two pressure sensors, as seen in Figure 11. The diffusion rates, shown in Figure 12, contain the decreasing pressure in the fore chamber for each of the four noble gases used in the experiment. In Figure 12, the data collection began where the fore pressure reached 600 *Torr* so they would be approximately on the same initial pressure scale. Where the cubes came to equilibrium varied due to varying starting pressures and the rate at which the gas was added to the fore pressure chamber. Figure 13 displays the reciprocal of the fore pressure data, which is used to extract the viscosity of the gas. This is the first step in the analysis to determine the viscosities of each gas as it flows through the glass rod. Once the viscosities are calculated for the volumetric parameters of the system, assumptions can be made about flow velocities and the associated propagating profile distributions. These characteristics are important in determining which gas would be most suitable to be used as a potential carrier of rubidium vapor atoms through the capillary tube. In the initial seconds of the inverse pressure rates, where the slopes ap-

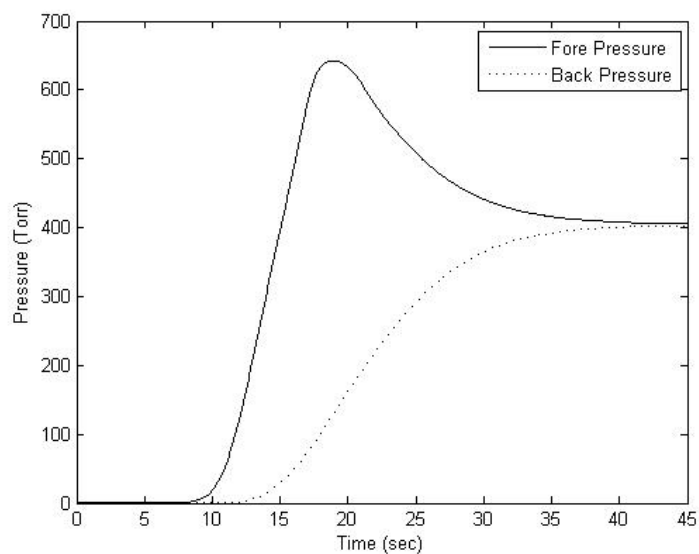


Figure 11. Pressure readings from the fore and back pressure chambers as approximately 600 Torr of krypton was added to the fore pressure cube and diffused to the back pressure chamber. Where the cubes came to equilibrium varied due to varying starting pressures and the rate at which the gas was added to the fore pressure chamber.

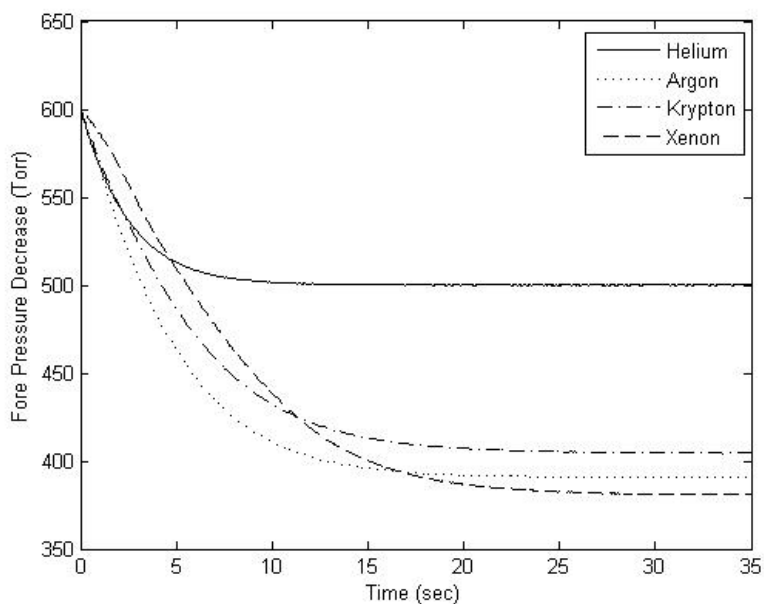
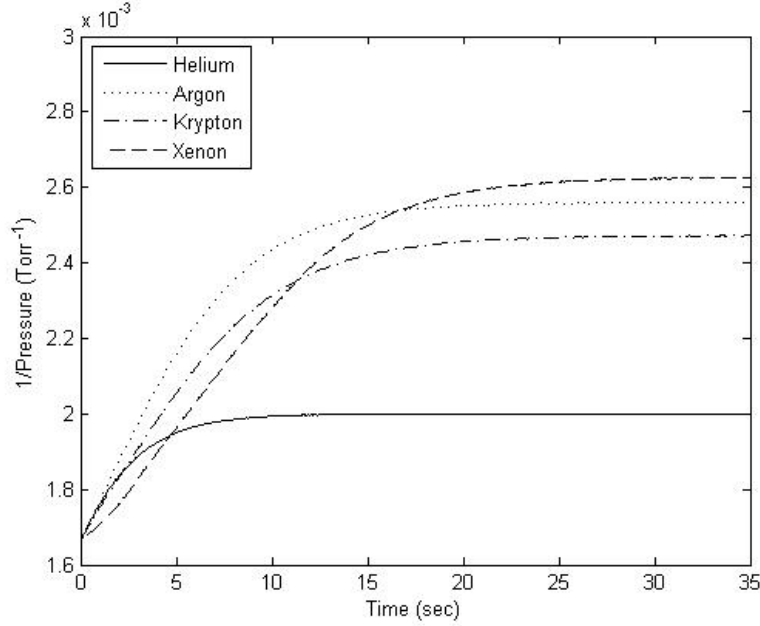


Figure 12. Fore pressure decrease data as the noble gases diffused through the glass rod to the back pressure chamber. Each gas data set starts at approximately 600 Torr in order to have the same relative initial pressure scale.



**Figure 13.** The inverse fore pressure data for each of the used noble gases.

pear to be nearly linear, the data was fit to a basic  $y = mx + b$  linear equation as seen in Figure 14. The linear regime was selected where the residual was nearly zero over the longest period of time. Least-Squares linear regression provided minimal residual to the fit compared to the attempted Levenberg-Marquardt and Gauss-Newton methods. The fit with residuals are shown in Figure 15. The slopes were inserted into equation (19) as the time dependant derivative of the inverse fore pressure and the viscosities for each noble gas were extracted and compared to previously recorded values by NIST, as seen in Table 2.

Establishing the viscosities by fitting the linear portion of the experimental inverse fore pressure data was an approach used in previous literature. The linear fitting technique assumes  $p_1 \gg p_2$ . However, including the back pressure measurements considers all the physical properties occurring on both ends of the capillary tube and provides more information about the flow. equation (22) explores all of the fluid

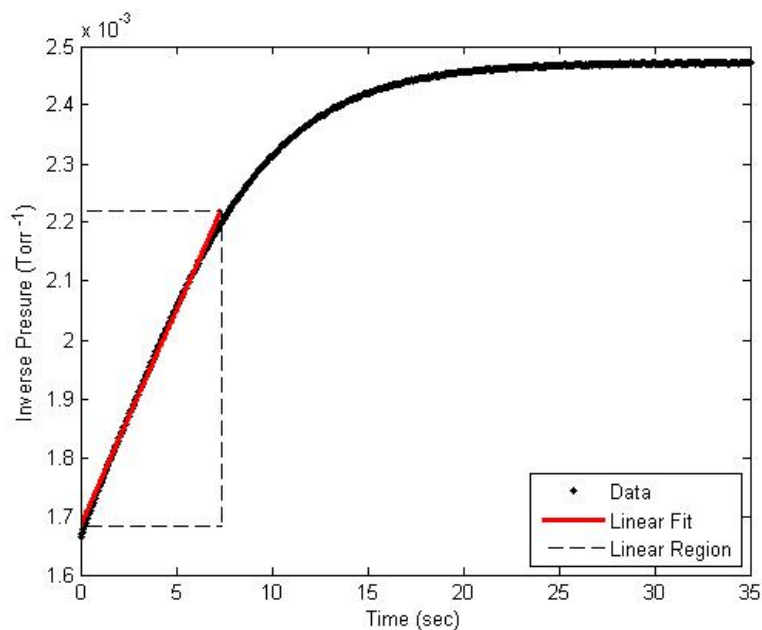


Figure 14. Inverse fore pressure data was fit to a  $y = mx + b$  linear equation for krypton. The slope of the fit equation was used to determine the viscosity of the flowing gas within the capillary tube. The data inside the dashed box represents the region that was appeared nearly linear.

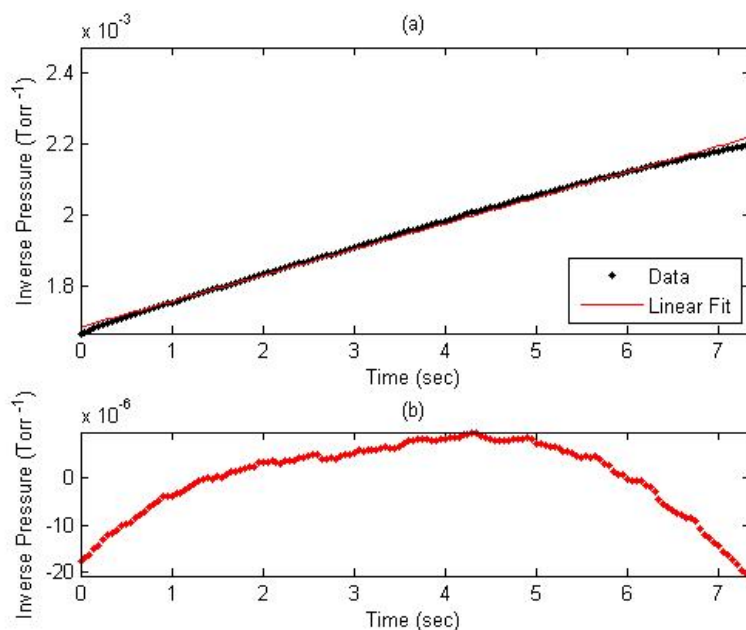


Figure 15. (a) Linear fit to krypton experimental inverse fore pressure data using the Least-Squares linear regression method. (b) Residual between the raw data and the best fit line.

**Table 2. The viscosities for fitting the slope, fitting the entire curve and the previous results recorded by NIST are shown in  $\mu Pa - Sec$ .**

Noble Gas	Slope Fit	Curve Fit	NIST Results
Helium	$61.310 \pm 1.566$	$5.420 \pm 0.238$	$19.838 \pm 1.984$
Argon	$53.254 \pm 1.213$	$20.604 \pm 0.251$	$22.543 \pm 2.254$
Krypton	$73.405 \pm 2.187$	$22.912 \pm 0.259$	$25.111 \pm 2.511$
Xenon	$82.934 \pm 0.919$	$36.719 \pm 0.281$	$22.945 \pm 2.295$

dynamics occurring in the system for any pressure differential. The fact that the back pressure began to increase before the gas inflow was closed off was neglected in the linear fit analysis. However, the back pressure employs a significant role when fitting the entire inverse fore pressure curve. The definition of the total pressure in the system is sum of the pressures contained in both chambers. When the gas began entering the fore pressure chamber, the diffusion process had already commenced because there was no shut-off valve between the two chambers. To accommodate this situation, the initial back pressure was subtracted from all of the fore pressure values confirming equation (21). From the solution to equation (24), the Least-Squares method was utilized to fit the entire experimental inverse fore pressure curves with two fit parameters. A demonstrated fit along with residuals between the data and the fit is shown in Figure 16. The fit parameter,  $\Gamma$ , was then substituted into equation (25) and the viscosities for each gas were determined. The viscosities for the linear fit and the ODE curve fit were converted to the commonly published units of  $\mu Pa - Sec$ , as seen in Table 2. By fitting the entire ODE characterizing all the fluid dynamics of the system rather than exclusively the linear segment of the inverse fore pressure yields viscosity measurements closer to the previously published values.

In order to understand the type of flow, laminar or turbulent, occurring within the glass rod, the Reynolds Number must be determined. Back pressures for each experiment were subtracted from the fore pressures to find the actual pressure gradient

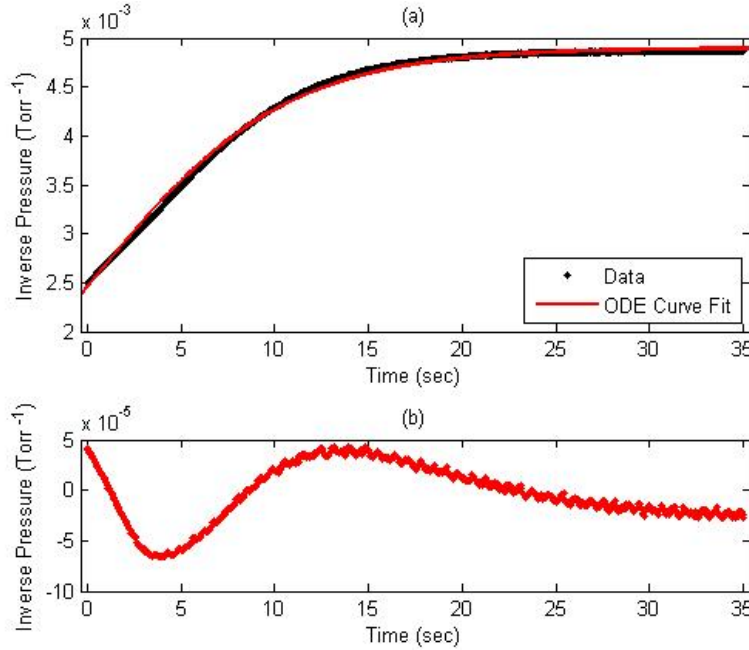


**Figure 16. (a) ODE curve fit to krypton experimental inverse fore pressure data using the Least-Squares linear regression method. (b) Residual between the raw data and the best fit curve.**

at each point in time. This determines the maximum flow velocity in equation (30), which will assist in choosing a carrier gas. Using the density of each gas at room temperature and resolved viscosities, the Reynolds Numbers can be calculated with equation (27). Figure 17 and Figure 18 display the Reynolds Number for each gas at every pressure differential for the viscosities extracted from the linear fit and the ODE fit, respectively.

If the Reynolds Number is less than approximately 30, then the flow through the tube can be assumed to follow Poiseuille flow theory. When the Reynolds Number is greater than 30, this simply means the gas does not enter the tube with a parabolic velocity profile described in equation (7). If the flow is turbulent, determining the flow distribution profiles and velocities becomes a non-trivial procedure. At some length down the tube, the flow distribution may develop into a Poiseuille flow model and the velocity profiles can be extracted. The length down the tube from the gas entry



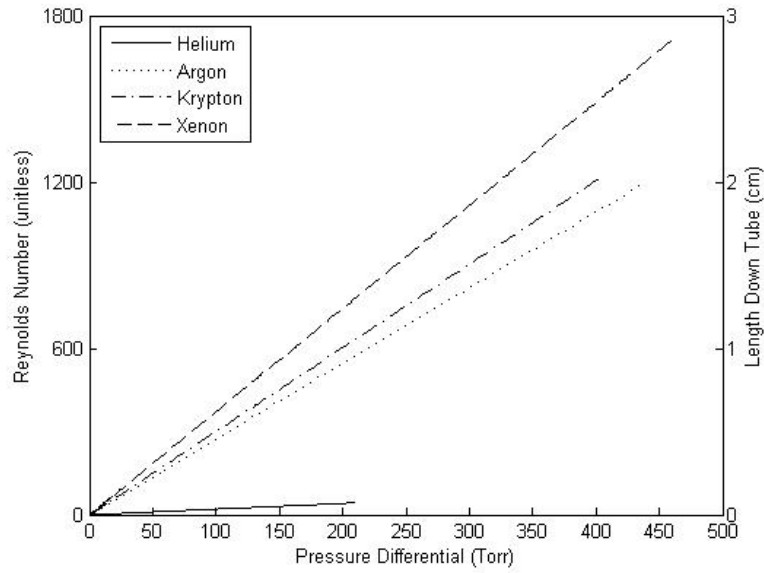


Figure 17. Left Axis: Reynolds Number at each pressure differential for each of the noble gases using the linear fit viscosity value. Right Axis: Length down the 12 cm tube before Poiseuille flow theory can be applied and the parabolic velocity profile is fully developed.

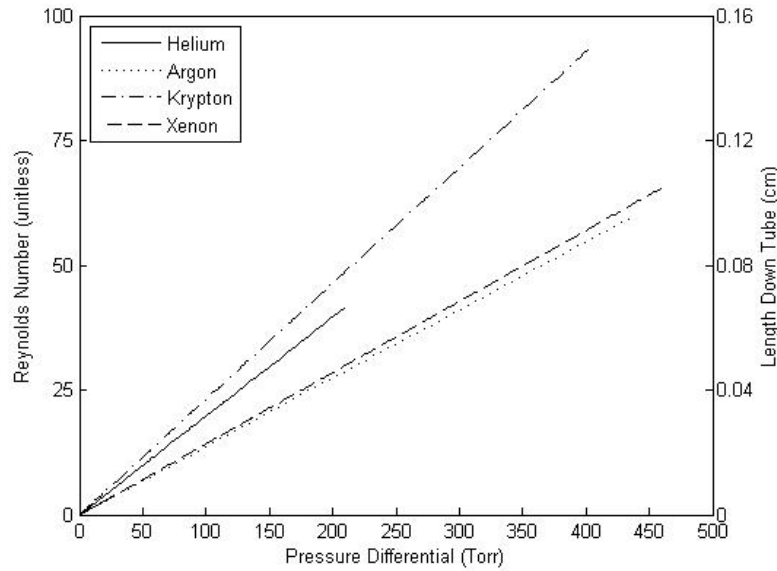
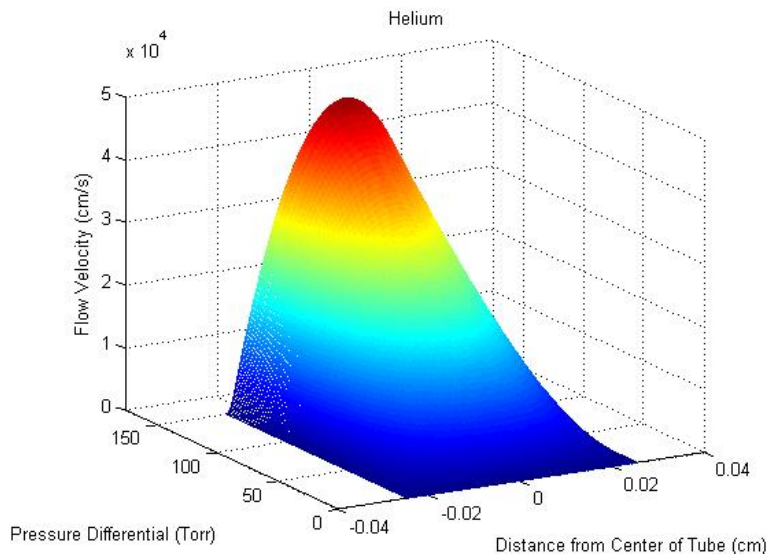


Figure 18. Left Axis: Reynolds Number at each pressure differential for each of the noble gases using the ODE curve fit viscosity value. Right Axis: Length down the 12 cm tube before Poiseuille flow theory can be applied and the parabolic velocity profile is fully developed.

point that Poiseuille theory applies is found by using equation (29). From the results shown in Figure 17 following the linear fit method, it can be seen that Poiseuille flow theory is only present within the tube for small pressure differentials ( $\Delta p < 10 \text{ Torr}$ ). The flow is then considered to be turbulent for 0.25 to almost 3 *cm* down the capillary for larger pressure differentials (with the exception of helium, which remains in the Poiseuille flow regime up to a 146 *Torr* pressure differential). The length of the capillary was measured to be 12 *cm* long, revealing 25% of the tube is under unpredictable and chaotic turbulent flow. The viscosities determined by fitting the ODE curve produced Reynolds Numbers that were approximately a factor of two smaller than the ones calculated through the linear fit method, as seen in Figure 18. These Reynolds Numbers convey a larger pressure differential margin can be explored before turbulent flow is experienced. The accelerated routine of solely fitting the initial inverse pressure data produces larger viscosity values and in turn outputs larger Reynolds Numbers. The technique explored in this analysis achieved more precise viscosity measurements yielding lower Reynolds Numbers describing the flow through the capillary tube. Manifesting the differential equations describing the known dynamics of the system and formulating solutions that mapped experimental data proved to be a justifiable avenue and modeling the drastically chaotic turbulent behavior was avoided.

When considering techniques on transferring number densities of alkali vapor through the tube used in this experiment, one such technique that can be considered is adding one of the noble gasses and allowing diffusion to transfer the alkali. Maintaining a pressure differential between the two chambers less than 150 *Torr* permits an accurate description of the flow velocity (without any alkali) through the tube. The velocity flow distributions under Poiseuille flow theory coincide with equation (7) where the profile of the gas propagating through the tube can be described by



**Figure 19. Velocity profile distribution for helium as a function of distance from the center of the glass rod,  $r$ , and for the pressure differentials that follow Poiseuille flow theory determined by the Reynolds Number being less than 30.**

a parabola. The flow velocity gradient is determined from equation (7) as a function of  $r$ , the distance from the center of the tube. Figure 19 through Figure 22 maps out the velocity profiles for each gas as a function of distance from the center of the tube only when the flow through the tube is described by 100% Poiseuille flow theory determined from fitting the ODE as displayed in Figure 18.

Transferring alkali through small inner-diameter tubes has been considered to be a time consuming procedure because previous techniques use basic diffusion (with no pumping or carrier gases used) and work on a time scale of weeks or even months to provide sufficient results. By applying a noble gas to assist in the propagation process, the window of time can be decreased dramatically. From the flow velocity results, helium propagates with the largest velocity through the tube with a flow that can be fully understood for a restricted pressure differential regime.

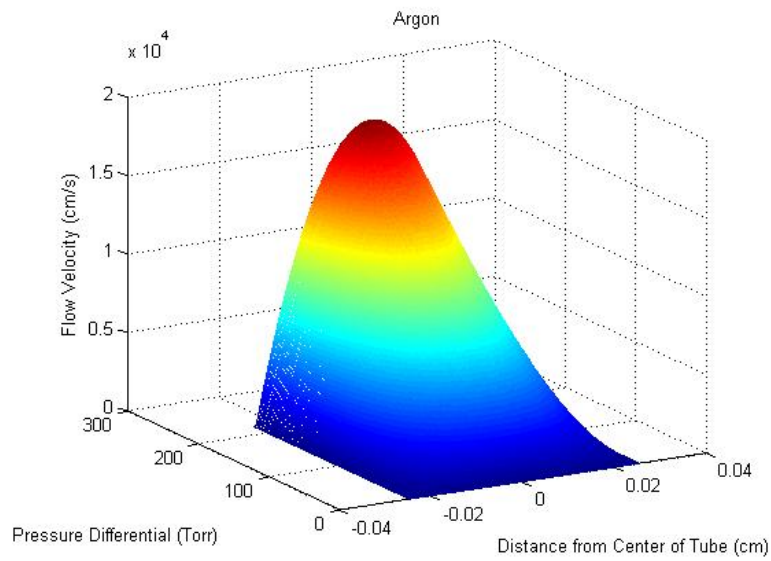


**Figure 20.** Velocity profile distribution for argon as a function of distance from the center of the glass rod,  $r$ , and for the pressure differentials that follow Poiseuille flow theory determined by the Reynolds Number being less than 30.

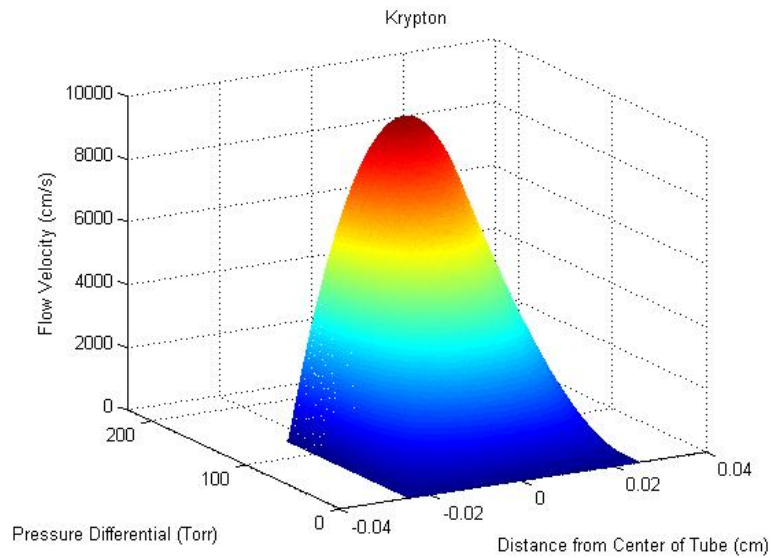


**Figure 21.** Velocity profile distribution for krypton as a function of distance from the center of the glass rod,  $r$ , and for the pressure differentials that follow Poiseuille flow theory determined by the Reynolds Number being less than 30.

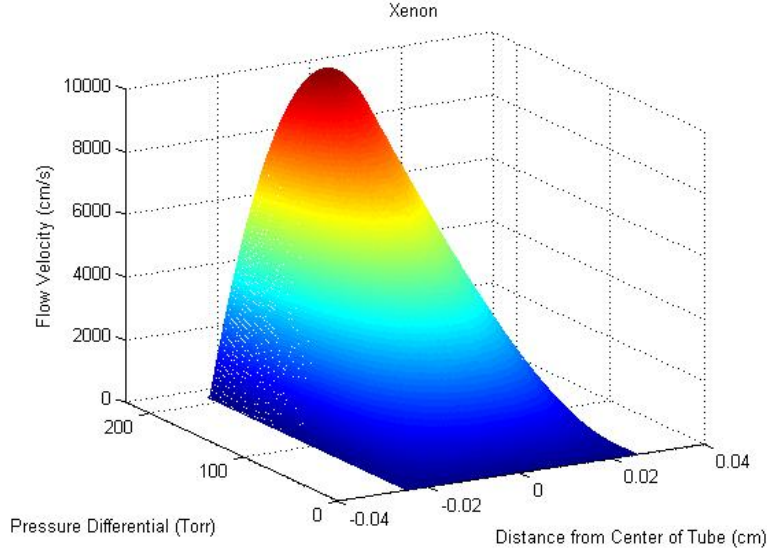


**Figure 22. Velocity profile distribution for xenon as a function of distance from the center of the glass rod,  $r$ , and for the pressure differentials that follow Poiseuille flow theory determined by the Reynolds Number being less than 30.**

## Rubidium Number Densities

First attempts to transfer rubidium vapor through the  $500\ \mu\text{m}$  capillary tube consisted of pumping on the back pressure chamber with the turbo pump. The system was heated to  $150\ \text{C}$  to generate a rubidium vapor in the fore pressure cube. A carrier gas was not introduced for this procedure with the anticipation that rubidium atoms would propagate through the tube with  $60\ \text{nTorr}$  in the aft chamber. The capillary tube used was  $20\ \text{cm}$  in length and the ends of the tubes were approximately  $1\ \text{cm}$  from the edges of the cubes, shown previously in Figure 9a. Scanning diode laser beams were directed slightly above the capillary tube searching for the rubidium  $\text{D}_1$  absorption spectrum, displayed in Figure 9b. A significant spectrum was extracted on the fore pressure chamber when the system was heated, but there was no trace of a spectrum on the back pressure chamber. Recognizing the time constraints of the project, an alternate technique was deployed after five days of pumping with no

apparent visible spectrum.

Importing a carrier gas was the next technique examined. Heat tape was wrapped around the main bus importing the noble gases to avoid changing the temperature within the chamber system. Approximately 40 to 80 *Torr* of krypton was added to the fore pressure chamber with no pumping mechanism on the back pressure chamber. After the gas diffused through the capillary into the back pressure cube, the gas was slowly released to the pumping system and the process was repeated. On the fifth day of practicing this approach, the fore pressure chamber held a constant pressure of 40 *Torr* while the back side cube maintained a pressure of a few *mTorr*. This proposed an apparent blockage within the capillary and discontinuing the efforts of diffusing rubidium vapor with a carrier gas. The entire system was disassembled to be disinfected and rebuilt. During the procedure of dismantling the apparatus, a visible magnitude of rubidium accumulation was discovered on the calcium fluoride window nearest to the exit of the tube in the back pressure chamber, as seen in Figure 23. The deposit formed a 1 *cm* diameter circle on the window and developed a raised conical formation in the center with a FWHM of approximately 0.05 *cm*.

Immediately after removing the capillary from the chamber the mass was recorded to be 13.899 *grams*. Directing a white LED source axially down the length of the tube exposed rubidium formations from the scattering light (not from fluorescence), displayed in Figure 24 and Figure 25. Ethanol was injected into the tube cleansing it of nearly all inhabiting contaminants and was then dried by heat enforcement. The mass of the evacuated tube was measured again at 13.893 *grams*, revealing approximately 6 *milligrams* of substance within the tube, which makes up 9.92% of total volume of the tube. This evidence proposes that as the rubidium/krypton mixture propagated through the tube, atoms were adhering to the inner walls of the capillary. If the rubidium volume to tube volume ratio increases over time, yielding more



**Figure 23.** Visible rubidium accumulation (with an outer diameter of 1 *cm* with a raised cone in the center having a FWHM of approximately 0.05 *cm*) on the calcium fluoride window closest to the exit of the capillary on the pump side chamber. The end of the tube was positioned about 1 *cm* away from the window and is shown in Figure 9. This validates rubidium successfully transferred through the 20 *cm* long, 500  $\mu\text{m}$  inner-diameter capillary tube.

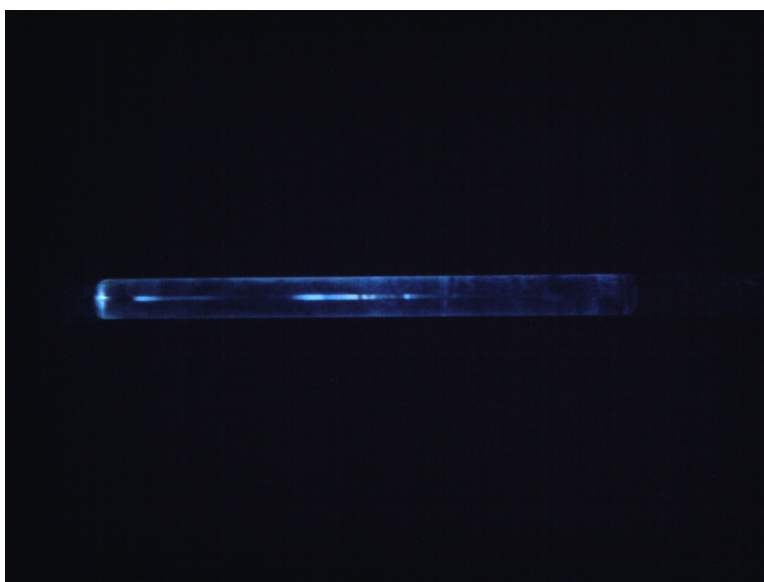


**Figure 24.** A white LED source was directed down the length of the capillary tube exposing rubidium deposits within the tube through scatter light effects (not fluorescence).

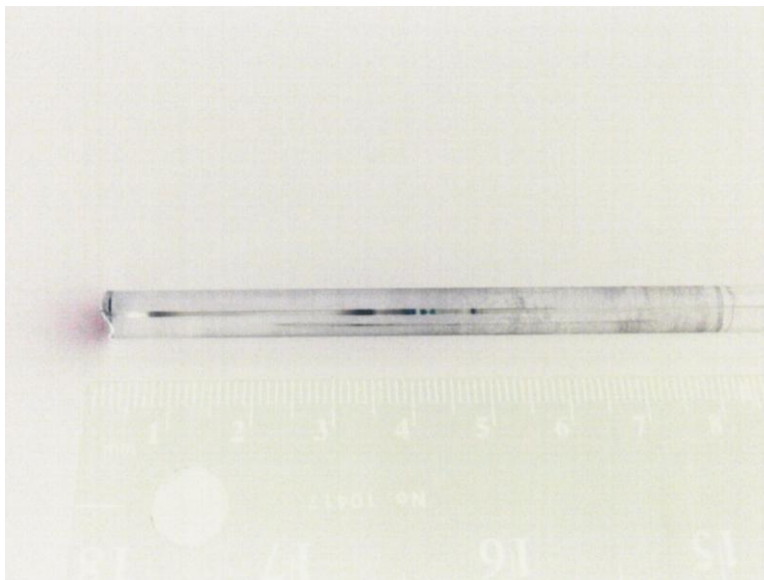


**Figure 25. Color inverted image of Figure 24 displaying rubidium deposits within the capillary through scatter light effects (not fluorescence) from a white LED source.**

atomic layers condensing to the walls of the tube, the flow rates will decrease. This is because the volumetric flow rate is proportional to  $R^4$ , shown in equation (10), which will make the task of transferring rubidium near impossible. The agents responsible for the agglomeration were postulated to be derivatives of oxidized substances residing within the tube after the manufacture process. Decontamination procedures were exerted prior to the experiments by heating and pumping down the system for several days. Further cleansing methods should be formulated in future work to prevent such circumstances.

New approaches were developed striving for a successful rubidium absorption spectrum. The length of the capillary tube was decreased to 12 *cm* and the ends of the tube were localized to the center of each chamber rather than close proximity to the edges of the cubes, shown in Figure 10a. This would decrease the diffusion time. Also, with the ends of the tube in the center of the pressure chambers, the scanning laser sources could be directed approximately 0.5 *cm* from the entrance and exit holes of the



capillary, shown in Figure 10b. Probing the endpoints of the tube allow a spectrum to be acquired from any alkali vapor flowing through the tube. From the previous two techniques, exclusively pumping with no carrier gas and basic diffusion, the remedy for successfully transferring rubidium through the tube was realized. From the fluid dynamical analysis, helium proved to implement the highest flow velocity with a vast permissible pressure differential margin while being constrained by the Poiseuille flow limits. Remaining within the Poiseuille flow regime ensured no chaotic flow was occurring that could produce phenomena like shock waves that might solidify the alkali in the capillary. With the vacuum pump slightly opened, a needle valve controlling the warm helium source was turned such that a slow steady constant flow of gas was being introduced to the system. A constant pressure gradient of approximately 80 *Torr* was maintained throughout this procedure. Continuously flowing the rubidium/helium combination through the system furnished fruitful results. An absorption spectrum representing the D<sub>1</sub> atomic hyperfine transitions for both isotopes of rubidium were revealed, shown in Figure 26. Changing the pressure gradient across the capillary increased the flow of alkali vapor resulting in larger number densities and the peaks became even more evident as seen in Figure 27 and Figure 28 for pressure gradients of approximately 120 and 150 *Torr*, respectively.

In order to determine the number density of the alkali vapor that transferred into the back pressure chamber, a summation of Voigt profiles was developed to fit the four hyperfine transitions for each of the isotopes using equation (46). If the laser probe has an intensity greater than the saturation intensity ( $I/I_{sat} > 1$ ), the incident intensity is considered a pump source rather than a probe. Because of this condition, atoms excited to an upper hyperfine component may relax to a different hyperfine ground state energy level than which it initially started due to spontaneous or stimulated emission. For example, if the  $F'' = 2 \rightarrow F' = 3$  transition in <sup>85</sup>Rb is

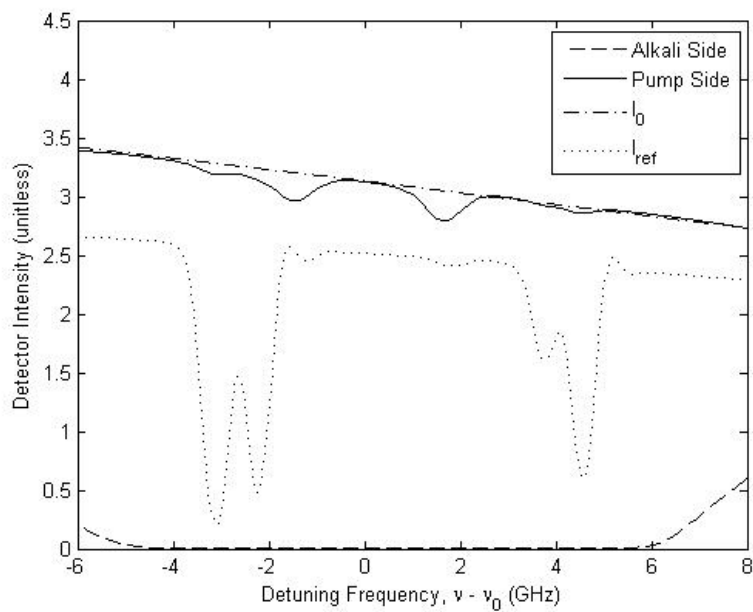


**Figure 26.** Atomic rubidium absorption peaks being collected from the back pressure chamber. Results accomplished by maintaining a constant pressure gradient of 80 *Torr* across the capillary tube with a constant input flow of helium in the fore pressure chamber and the vacuum pump slightly opened in the back pressure chamber.

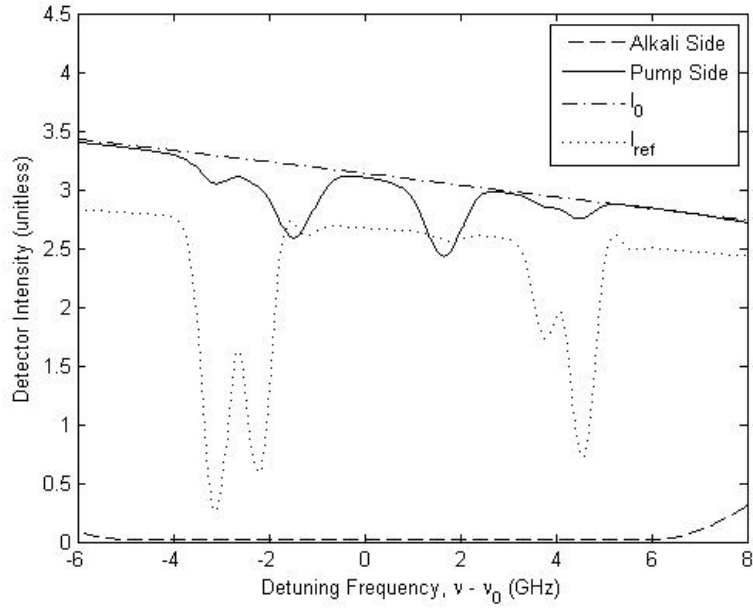


Figure 27. Atomic absorption peaks being collected from the back pressure chamber. A pressure gradient of approximately 120 Torr was established to increase the number density flowing through the capillary.

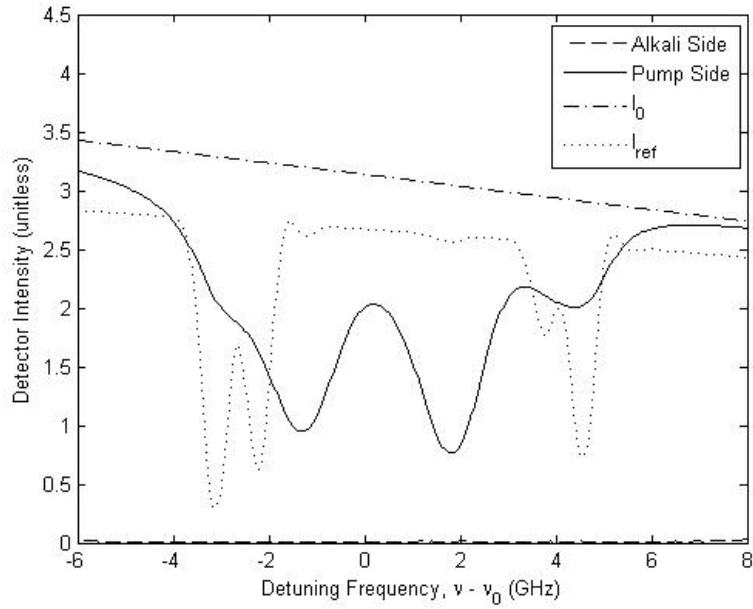
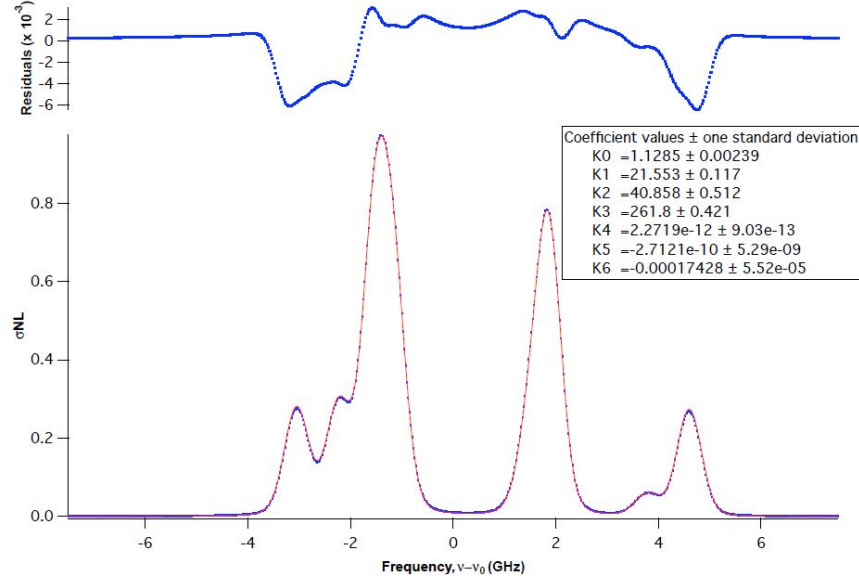


Figure 28. Atomic absorption peaks being collected from the back pressure chamber. A pressure gradient of approximately 150 Torr was established to increase the number density flowing through the capillary.



**Figure 29.** Fit to the multi-isotopic rubidium absorbance spectrum that was transferred through the capillary tube and into the pump chamber along with residuals displaying the difference between the fit (red) and the raw data (blue) with  $\Delta P = 120\text{Torr}$ .

optically pumped, the atom may relax to the lower  $F'' = 3$  ground state rather than the  $F'' = 2$  state. By depleting the hyperfine ground state being investigated directly effects the predicted Boltzmann distribution in equation (44). This will change the relative amplitude of the interrogated transition and the practice of fitting the Voigt profiles will become difficult. From the spectrum fit in Figure 29, the residual is calculated by subtracting the fit from the data. The fit amplitudes are larger than the raw data amplitudes only for the  $^{87}\text{Rb}$  hyperfine structure, but are smaller than the data for the  $^{85}\text{Rb}$  spectrum (see fit and residual in Figure 29). It can be inferred that the isotopic ratio has changed from the naturally occurring abundances previously stated. The  $^{87}\text{Rb}$  atom has a larger mass than the  $^{85}\text{Rb}$  atom. Because of the mass difference the heavier atoms have different flow characteristics than the lighter atoms. To estimate number densities with more precision, further analysis must be conducted to investigate the isotopic ratio shift. For the case of this experiment, the number

densities will only be slightly effected and the focus was to approximate a number density for fiber laser applications.

The absorbance is dependant on the path length of the test cell. Since this experiment demonstrates a constant flow of alkali rather than a cell under equilibrium conditions, the path length depends on the distance away from the end of the tube the probe is investigating. The flow of rubidium exiting the capillary is modeled by a constant diverging cone. The FWHM of the deposit on the window is approximately 0.05 *cm* in diameter. Determining an interaction path length from this criteria was determined for three locations by mapping a constant diverging cone from the exit of the tube to the deposit. The first location dissected the cone immediately after the rubidium exited the tube where the path length equals the 0.05 *cm* diameter of the tube. The second location of 0.15 *cm* was determined from the FWHM of the rubidium deposit on the window of the cell. The probe was aimed 1.0 *cm* away from the end of the tube which is the same distance the tube was when the rubidium accumulated on the window. The third case used the width of the chamber, 7.0 *cm*, investigating the maximum distance away from the tube.

The Gaussian and Lorentzian lineshape widths were permitted to vary in the fit because the  $I/I_{sat}$  condition altered the population of the hyperfine ground states which directly effects the Boltzmann distribution. From Figure 29, the constant  $K0$  represents the total amplitude of the profile,  $K1$  represents the frequency shift,  $K2$  represents the Lorentzian width,  $K3$  represents the Gaussian width, and the constants  $K4$  through  $K6$  represent a quadratic baseline on either side of the profile distribution for a better fit  $((K4)\nu^2 + (K5)\nu + (K6))$ . The absorbance amplitude is determined by a normalization factor of  $\sqrt{\pi}/\sqrt{\ln 2}$  which is multiplied by the profile amplitude fit parameter ( $K0$ ). The number density is calculated by dividing the absorbance amplitude by  $(l\lambda_0^2)/(8\pi\tau_{21})$ . The calculated number densities associated

with path length are shown in Table 3. A rubidium vapor pressure can be determined

**Table 3. Calculated rubidium number densities for the absorbance data fit in Figure 29 with  $\Delta P = 120 \text{ Torr}$  and estimated path lengths.**

Path Length ( <i>cm</i> )	Number Density ( $\text{cm}^{-3}$ )	Error ( $\text{cm}^{-3}$ )
0.05	$1.384\,657 \times 10^{12}$	$2.796\,86 \times 10^{10}$
0.15	$4.615\,525 \times 10^{11}$	$3.342\,76 \times 10^9$
7.00	$9.890\,410 \times 10^9$	$3.135\,48 \times 10^7$

using the calculated number densities for the three interaction path lengths previously discussed. The back chamber maintained a total pressure of 20 *Torr*. A mixing ratio was determined by dividing the rubidium vapor pressure by the total pressure in the chamber. The mixing ratios are shown in Table 4. A rubidium vapor pressure

**Table 4. Mixing ratios between the rubidium and helium combinations are given for the three interaction path lengths which determined the rubidium number densities that propagated through the capillary tube.**

Path Length ( <i>cm</i> )	Vapor Pressure ( <i>Torr</i> )	Mixing Ratio
0.05	$5.064 \times 10^{-5}$	2.532 <i>ppm</i>
0.15	$1.688 \times 10^{-5}$	0.844 <i>ppm</i>
7.00	$3.617 \times 10^{-7}$	18.085 <i>ppb</i>

was estimated to be  $5.664 \times 10^{-5}$  *Torr* using the temperature of the chamber, which was 353.15 *K*. The back pressure chamber maintained a total pressure of 140 *Torr*, providing a gas mixing ratio of 405 *ppb*. The smaller two interaction path lengths from Table 4 do not accurately quantify the mixing ratio throughout the back pressure chamber. However, the length of 7.00 *cm* is equivalent to the width of the chamber and can accurately describe the vapor pressure. When comparing the mixing ratio of the fore and back pressure chambers, it can be seen that the ratio on the fore pressure side is approximately 20 times larger than the gas ratio in the back pressure chamber. This concludes that a sufficient amount of rubidium is propagating through

the capillary tube to the back pressure chamber without condensing to the inner walls to the point where the radius of the tube is effecting the flow of the rubidium.

## V. Conclusions

### Fluid Dynamic Analysis

This work provided a thorough flow characterization of four noble gases to determine the gas viscosity and velocity profiles distributions. Previous techniques for extracting flow viscosities were explored and compared to an alternate approach. Considering the entire ordinary differential equation that contains the temporal back pressure measurements is critical in modeling the physical properties of the system. Once viscosity values were compared to recorded NIST values, Poiseuille flow theory was investigated. Following the constraints of Poiseuille flow allowed for a complete understanding of the velocity profile distribution throughout the capillary tube. Establishing the type of flow and velocities each gas experienced through the experiments aided in the selection process of which atoms could be used as carriers for the rubidium vapor. Avoiding chaotic turbulent flow was also valuable information ascertained from the flow experiments which could have lead to shock wave phenomena that could have dismantled the propagation flow. The Reynolds Number calculations outlined a pressure differential margin that would lead to a quicker transferring routine without altering the system parameters and apparatus.

### Transferring Rubidium Vapor Through a Capillary Tube

This work examined three techniques on how to transfer atomic rubidium vapor through a small inner-diameter capillary tube. Pumping on the system with a turbo pump proved to be a preliminary approach with no direct achievement, but portrayed a major role in depicting a successful route. Basic diffusion principals were followed by adding various pressures of krypton to the fore pressure chamber and allowing the system to come to equilibrium. An absorption spectrum was not extracted, but, a



visible conglomerate was evident on the window closest to the exit of the capillary. 6 *milligrams* of rubidium were removed from within the tube revealing evidence that a fraction of the propagating rubidium was adhering to the walls of the capillary. This could have developed through previous contamination of oxidation molecules inhabiting the tube from the time of manufacture to the time of implementation in the transferring apparatus. A combination of the two previous approaches was attempted and a D<sub>1</sub> rubidium absorption spectrum was obtained. From the measured spectrum, number densities of  $9.89 \times 10^{10} \text{ cm}^{-3}$  and  $5.5 \times 10^{10} \text{ cm}^{-3}$  were calculated for a path length of 7 *cm*. DPALs typically operate with number densities on the order of  $10^{13} \text{ cm}^{-3}$ , which is much larger than demonstrated here. These are preliminary techniques for advancing alkali vapor filled hollow-core fiber laser systems and new approaches are currently being explored.

## Future Work

Preparing the capillary tube for the experiment is an essential step when using atomic alkali. Alkali is highly reactive with any form of oxidation yielding emphases on decontamination procedures to evacuate the inner walls of the capillary. Contamination in an alkali cell spreads quickly bringing and abrupt halt to any existing experiments. Exploring what fraction of alkali naturally clings to the inner walls of the capillary would prove to be beneficial to ensure transferring techniques can be examined over long periods of time without the diameter of the tube closing and resisting vapor flow. Adapter fittings connecting various parts of the entire apparatus should be selected on the basis that they can be heated to high temperatures and cooled multiple times without generating a leak within the system. Varying the temperature could be effective if the option of solidifying the rubidium before evacuating the cell is preferred.

Measuring the exiting flow characteristics at the end of the tube would prove to be beneficial in extracting number densities within the chambers. Using an infrared camera to view the fluorescence given off by the resonating rubidium vapor atoms would provide a more accurate path length and more precisely predict the recorded number densities. Once a spectrum is extracted from the back pressure chamber and rubidium vapor is apparent on both ends of the capillary, alkali could be assumed to be within the tube. The number densities inside the tube are even more critical to the fiber laser community, especially for a diode pumped alkali fiber amplifier application. The capillary tube was solely employed as a surrogate to generate number densities within a small inner-diameter tube. Scaling down the inner-diameter should be examined providing thresholds on how small the diameter can be before alkali flow is restricted by the tube and what maximum number densities of various gases can be issued inside the tube for useful fiber laser applications.

A more precise measurement of the number density could be determined if the laser probe is investigating hyperfine transitions at an intensity that is less than the saturation intensity. By neglecting this criteria, the hyperfine ground state at line center is being depleted and the Maxwell Boltzmann distribution does not correctly model the relative amplitudes of the transitions. The flow of alkali vapor through a small inner diameter capillary tube should be accurately modeled for future work. Determining if the mass difference between isotopes plays an important role in the flow velocity could assist in understanding why the isotopic ratios were shifted in the rubidium spectrum.

## Appendix A. Fitting Inverse Pressure Curves

The inverse pressure curves were fit to two different equations. The linear equation assumes  $p_1 \gg p_2$  and fits the linear regime of the inverse pressure. The ODE fit includes all of the physical dynamics of the system and does not neglect the pressure on the back chamber. Figure 30 through Figure 33 show the linear regime fits with the residuals. Figure 34 through Figure 37 show the fit to the ODE with the residuals. Table 5 displays the fit parameters for the linear regime, specifically the slope of the line and the y-intercept that best fits the data using the Least-Squares linear regression method. Table 6 displays the fit constants that are directly related to the viscosity as well as the estimated total pressure constant.

**Table 5. Linear fit parameters determined from Least-Squares linear regression method.**

Noble Gas	Slope ( $(Torr - sec)^{-1}$ )	y-intercept ( $Torr^{-1}$ )
Helium	$8.723 \times 10^{-5}$	0.0017
Argon	$1.008 \times 10^{-4}$	0.0017
Krypton	$7.310 \times 10^{-5}$	0.0017
Xenon	$6.470 \times 10^{-5}$	0.0016

**Table 6. ODE fit parameters determined from Least-Squares linear regression method.**

Noble Gas	Total Pressure ( $p_0$ )	Constants ( $\Gamma$ )
Helium	216.344	0.428300
Argon	445.591	0.232063
Krypton	408.249	0.191210
Xenon	479.000	0.140000

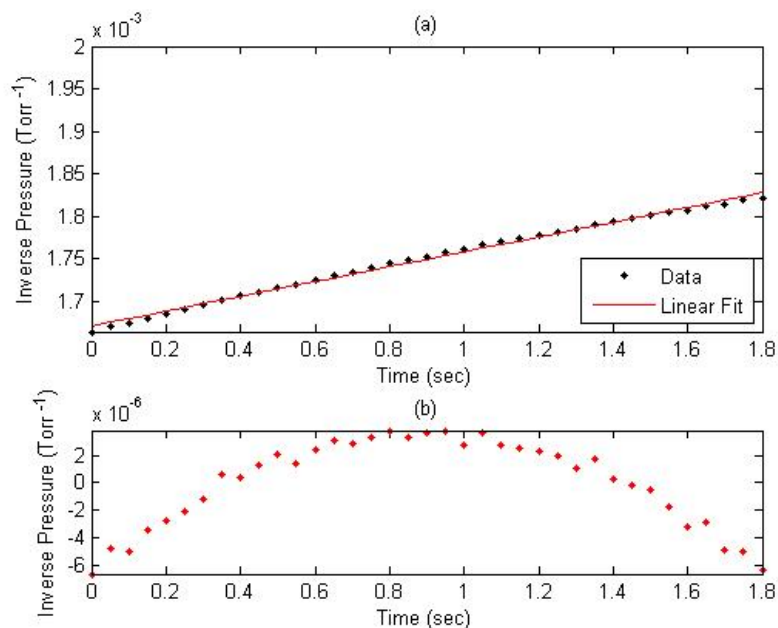


Figure 30. (a) Linear curve fit to helium experimental inverse fore pressure data using Least-Squares linear regression method. (b) Residual between the raw data and the best fit curve.

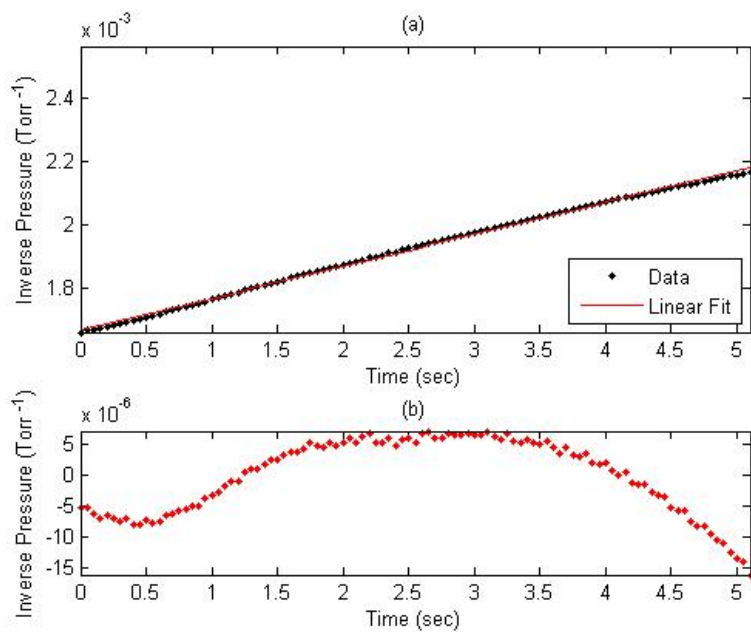


Figure 31. (a) Linear curve fit to argon experimental inverse fore pressure data using Least-Squares linear regression method. (b) Residual between the raw data and the best fit curve.

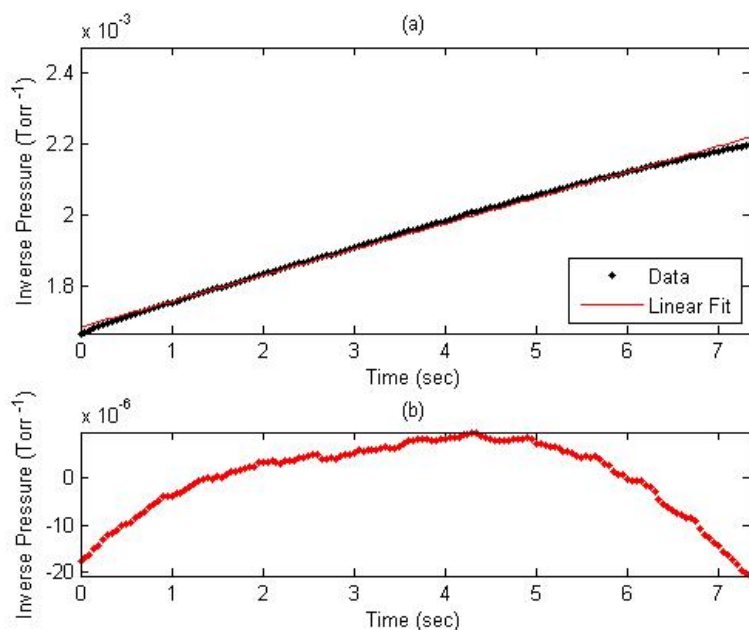


Figure 32. (a) Linear curve fit to krypton experimental inverse fore pressure data using Least-Squares linear regression method. (b) Residual between the raw data and the best fit curve.

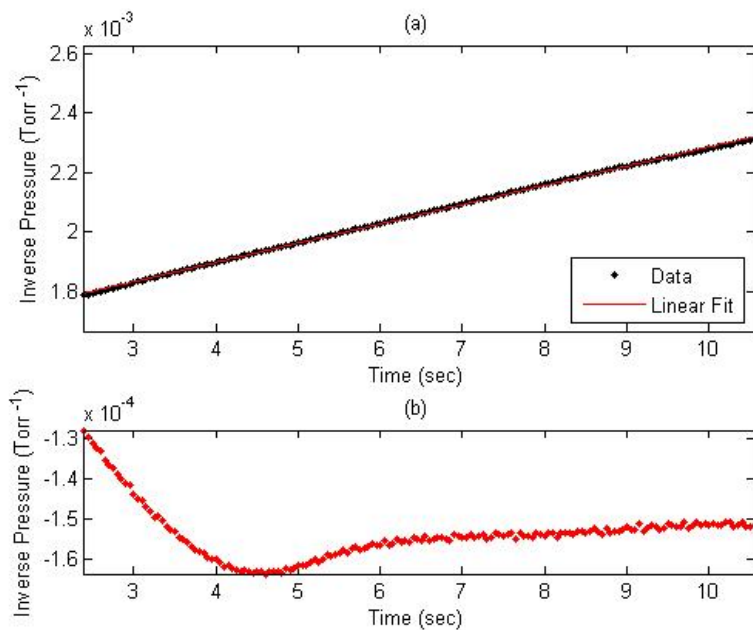


Figure 33. (a) Linear curve fit to xenon experimental inverse fore pressure data using Least-Squares linear regression method. (b) Residual between the raw data and the best fit curve.

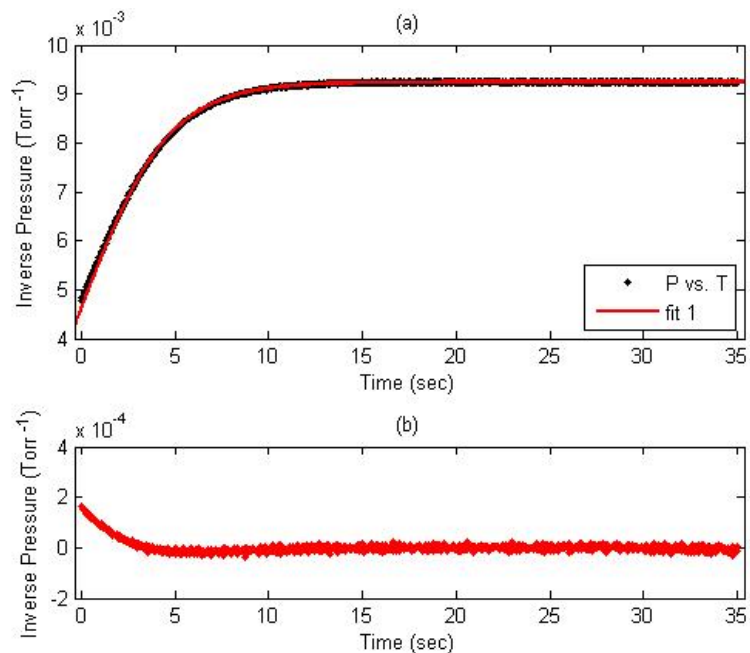


Figure 34. (a) ODE curve fit to helium experimental inverse fore pressure data using Least-Squares linear regression method. (b) Residual between the raw data and the best fit curve.

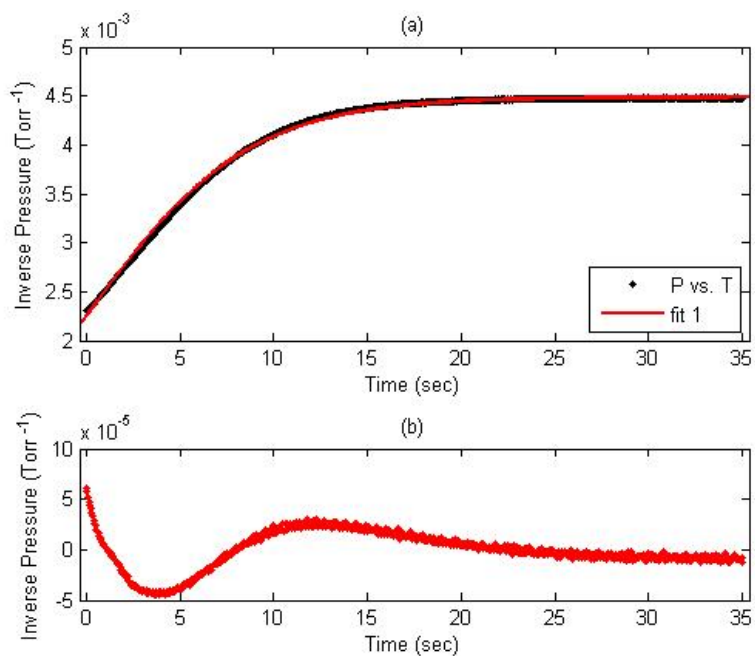


Figure 35. (a) ODE curve fit to argon experimental inverse fore pressure data using Least-Squares linear regression method. (b) Residual between the raw data and the best fit curve.

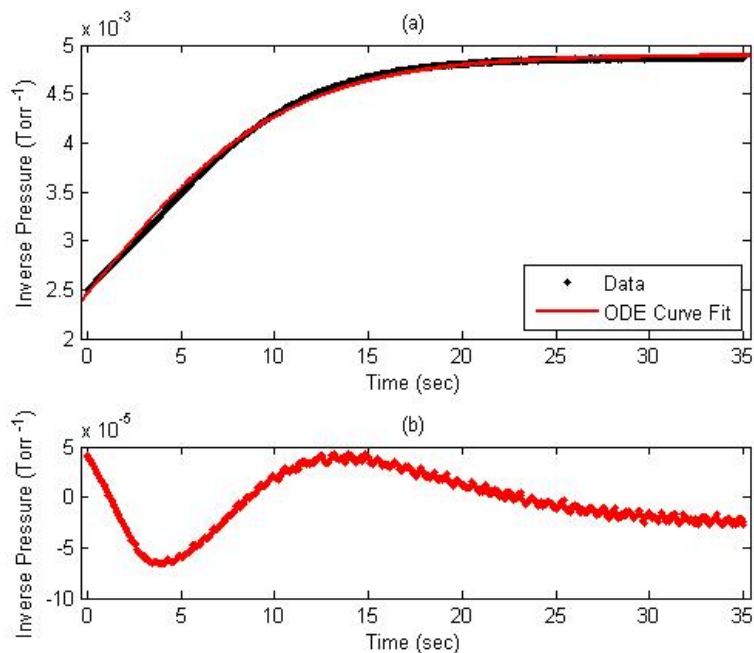


Figure 36. (a) ODE curve fit to krypton experimental inverse fore pressure data using Least-Squares linear regression method. (b) Residual between the raw data and the best fit curve.

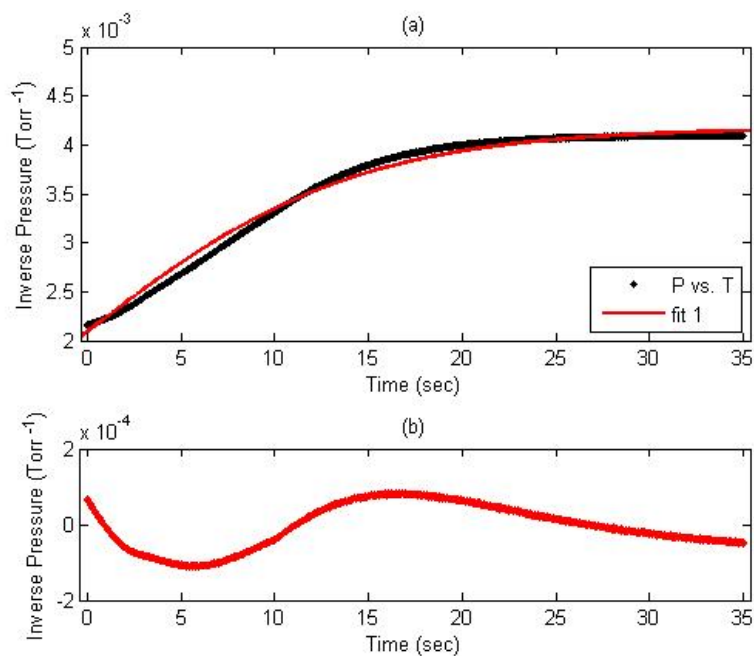


Figure 37. (a) ODE curve fit to xenon experimental inverse fore pressure data using Least-Squares linear regression method. (b) Residual between the raw data and the best fit curve.

## Bibliography

- [1] Bernath, Peter F. *Spectra of Atoms and Molecules*, Oxford University Press, New York, NY, 1995.
- [2] Hostutler, David A. *Power Enhancement of a Rubidium Vapor Laser with a Master Oscillator Power Amplifier*, Optics Express, Vol. 16, No. 11, May 2008.
- [3] Jin, Wei, Xin Shi, Xinbing Wang, and M. Süleyman Demokan, *Gas discharge in hollow-core fibers*, SPIE Newsroom, 10.1117/2.1200802.1071, 2008.
- [4] Jones, Andrew M., A. V. Vasudevan Nampoothiri, Amarin Ratanavis, Rajesh Kadel, Natalie V. Wheeler, François Couny, Fetah Benabid, Wolfgang Rudolph, Brian R. Washburn, and Kristan L. Corwin, *C<sub>2</sub>H<sub>2</sub> Gas Laser Inside Hollow-Core Photonic Crystal Fiber Based on Population Inversion*, IEEE, 978-1-55752-890-2/10, 2010.
- [5] Moore, Walter J. *Physical Chemistry*. 4th Ed., Prentice Hall, Englewoods Cliffs, NJ, 1972, pp152-154.
- [6] Polik, William F. *Physical Chemistry I Lab Manual*. Hope College, Holland, MI, 2010, section C2.
- [7] Slepko, Aaron D., Amar R. Bhagwat, Vivek Venkataraman, Pablo Londero, and Alexander L. Gaeta, *Generation of large alkali vapor densities inside bare hollow-core photonic band-gap fibers*, Optics Express, Vol. 16, No. 23, 18976-18983, 2008.
- [8] Smith, P. W., *A waveguide gas laser*, Applied Physics Letter 19, pp. 132-134, 1971.
- [9] Steck, Daniel A. "<http://steck.us/alkalidata>".
- [10] Tritton, D.J. *Physical Fluid Dynamics*, Van Nostrand Reinhold Company Ltd., 1977.
- [11] White, Frank M. *Viscous Fluid Flow*, McGraw-Hill International Editions, 1991.



REPORT DOCUMENTATION PAGE				Form Approved OMB No. 074-0188	
<p>The public reporting burden for this collection of information is estimated to average 1 hour per response, including the time for reviewing instructions, searching existing data sources, gathering and maintaining the data needed, and completing and reviewing the collection of information. Send comments regarding this burden estimate or any other aspect of the collection of information, including suggestions for reducing this burden to Department of Defense, Washington Headquarters Services, Directorate for Information Operations and Reports (0704-0188), 1215 Jefferson Davis Highway, Suite 1204, Arlington, VA 22202-4302. Respondents should be aware that notwithstanding any other provision of law, no person shall be subject to a penalty for failing to comply with a collection of information if it does not display a currently valid OMB control number.</p> <p><b>PLEASE DO NOT RETURN YOUR FORM TO THE ABOVE ADDRESS.</b></p>					
1. REPORT DATE (DD-MM-YYYY) 24-03-2011		2. REPORT TYPE Master's Thesis		3. DATES COVERED (From – To) Oct 2010 – Dec 2010	
4. TITLE AND SUBTITLE Diffusion of Rubidium Vapor through Hollow-Core Fibers for Gas-Phased Fiber-Lasers				5a. CONTRACT NUMBER	
				5b. GRANT NUMBER	
				5c. PROGRAM ELEMENT NUMBER	
6. AUTHOR(S) Guild, Eric M., Civilian				5d. PROJECT NUMBER	
				5e. TASK NUMBER	
				5f. WORK UNIT NUMBER	
7. PERFORMING ORGANIZATION NAMES(S) AND ADDRESS(S) Air Force Institute of Technology Graduate School of Engineering and Management (AFIT/EN) 2950 Hobson Way WPAFB, OH 45433-7765				8. PERFORMING ORGANIZATION REPORT NUMBER AFIT/OSE/ENP/11-M01	
9. SPONSORING/MONITORING AGENCY NAME(S) AND ADDRESS(ES) HEL-JTO (Dr. Harro Ackermann) 901 University Blvd SE Suite 100 Albuquerque, NM 87106 (505) 248-8208 harro.ackermann@JTO.HPC.MIL				10. SPONSOR/MONITOR'S ACRONYM(S) HEL-JTO	
				11. SPONSOR/MONITOR'S REPORT NUMBER(S)	
12. DISTRIBUTION/AVAILABILITY STATEMENT APPROVED FOR PUBLIC RELEASE; DISTRIBUTION UNLIMITED					
13. SUPPLEMENTARY NOTES					
14. ABSTRACT <p>This work examines the diffusion of rubidium through a small diameter tube alone and in the presence of noble gases. A fluid dynamics analysis is investigated to aid in choosing a method for transferring atomic rubidium vapor that is reliable and efficient. Solutions to the time dependant ordinary differential equation describing the experimental flow properties of the system reveal more precise outcomes than previously practiced routines. Resolved viscosities and Poiseuille flow theory velocity profile distributions are characterized for noble gas carriers of the rubidium vapor. Applying Reynolds Numbers to the flow experiments provides pressure differential boundaries that are employed in the successful rubidium vapor transfer process. Atomic spectroscopy is demonstrated through the use of a rubidium D<sub>1</sub> resonate diode laser to record an absorption spectrum and extract alkali vapor densities that successfully propagated through a 12 cm long capillary tube with a 500 µm inner diameter. Rubidium number densities on the order of 1.384 x 10<sup>12</sup> cm<sup>-3</sup>, 4.615 x 10<sup>11</sup> cm<sup>-3</sup> and 9.890 x 10<sup>9</sup> cm<sup>-3</sup> were recorded for interaction path lengths of 0.05 cm, 0.15 cm and 7.0 cm, respectively. Number densities were achieved through the constant flow and diffusion of a helium/rubidium combination. Sustaining a constant pressure differential between 80 and 150 Torr across the capillary tube assisted in transferring the rubidium vapor through a small inner-diameter hollow-core tube.</p>					
15. SUBJECT TERMS					
16. SECURITY CLASSIFICATION OF:			17. LIMITATION OF ABSTRACT  UU	18. NUMBER OF PAGES  73	19a. NAME OF RESPONSIBLE PERSON Glen P. Perram, PhD (ENP)
REPORT U	ABSTRACT U	c. THIS PAGE U			19b. TELEPHONE NUMBER (Include area code) (937) 255-3636, x4504 glen.perram@afit.edu

Standard Form 298 (Rev. 8-98)

Prescribed by ANSI Std. Z39-18